Study of variability in long-term multiwavelength optical lightcurves of blazar AO 0235+164

Abhradeep Roy [ID],[1] Alok C. Gupta [ID],[2,3] Varsha R. Chitnis [ID],[1] Sergio A. Cellone [ID],[4,5] Claudia M. Raiteri [ID],[6] Gustavo E. Romero [ID],[7,5] Paul J. Wiita [ID],[8] Anshu Chatterjee [ID],[1] Jorge A. Combi [ID],[5,7,9] Mai Liao [ID],[10,11] Arkadipta Sarkar [ID],[12] and Massimo Villata [ID][6]

[1] Department of High Energy Physics, Tata Institute of Fundamental Research, Homi Bhabha Road, Mumbai-400005, India
[2] Aryabhatta Research Institute of Observational Sciences (ARIES), Manora Peak, Nainital 263001, India
[3] Key Laboratory for Research in Galaxies and Cosmology, Shanghai Astronomical Observatory, Chinese Academy of Sciences, Shanghai 200030, China
[4] Complejo Astronómico El Leoncito (CASLEO, CONICET-UNLP-UNC-UNSJ), San Juan, Argentina
[5] Facultad de Ciencias Astronómicas y Geofísicas, Universidad Nacional de La Plata, La Plata, Buenos Aires, Argentina
[6] INAF-Osservatorio Astrofisico di Torino, Via Osservatorio 20, I-10025 Pino Torinese, Italy
[7] Instituto Argentino de Radioastronomía (CCT-La Plata, CONICET; CICPBA; UNLP), Buenos Aires, Argentina
[8] Department of Physics, The College of New Jersey, 2000 Pennington Rd., Ewing, NJ 08628-0718, USA
[9] Deptamento de Ingeniería Mecánica y Minera, Universidad de Jaén, Campus Las Lagunillas s/n Ed. A3 Jaén, 23071, Spain
[10] CAS Key Laboratory for Researches in Galaxies and Cosmology, Department of Astronomy, University of Science and Technology of China, Hefei, Anhui 230026, China
[11] School of Astronomy and Space Science, University of Science and Technology of China, Hefei, Anhui 230026, China
[12] Deutsches Elektronen-Synchrotron, Platanenallee 6, D-15738 Zeuthen, Germany

ABSTRACT

We present a long-term and intraday variability study on optical multiwaveband ($UBVRI$) data from the blazar AO 0235+164 collected by various telescopes for $\sim$44 years (1975–2019). The blazar was found to be significantly variable over the years in all wavebands with a variation of about six magnitudes between its low and active states. The variations in the different wavebands are highly correlated without any time-lag. We did not observe any significant trend in color variation with time, but we observed a bluer-when-brighter trend between the $B - I$ color index and the R-magnitude. Optical BVR-band spectral energy distributions always show a convex shape. Significant intraday variability was frequently seen in the quasi-simultaneous observations of AO 0235+164 made on 22 nights in R and V-bands by the CASLEO and CAHA telescopes during 1999–2019. We also estimated the central supermassive black-hole mass of $7.9 \times 10^7 M_\odot$ by analyzing the broad Mg II emission line in AO 0235+164's spectrum. We briefly explore the probable physical scenarios responsible for the observed variability.

Keywords: galaxies: active – BL Lacertae objects: general – quasars: individual – BL Lacertae objects: individual: AO 0235+164

1. INTRODUCTION

Blazars belong to the radio-loud (RL) class of active galactic nuclei (AGNs). This extremely variable class is the union of BL Lacertae objects (BL Lacs) and flat spectrum radio quasars (FSRQs). Blazars host a large-scale relativistic jet of plasma pointing very close to the observer's line of sight (Urry & Padovani 1995). The jet is launched from the very near vicinity of the supermassive black hole (SMBH) of mass $10^6 - 10^{10}$ M$_\odot$ at the center of the AGN (e.g., Woo & Urry 2002). Blazars are characterized by highly variable emission throughout the whole electromagnetic (EM) spectrum, from radio to γ-rays, and their spectral energy distributions (SEDs) are characterized by two broad humps (Fossati et al. 1998). Blazars display high and vari-

Corresponding author: Abhradeep Roy
abhradeep.1996@gmail.com, abhradeep.roy@tifr.res.in
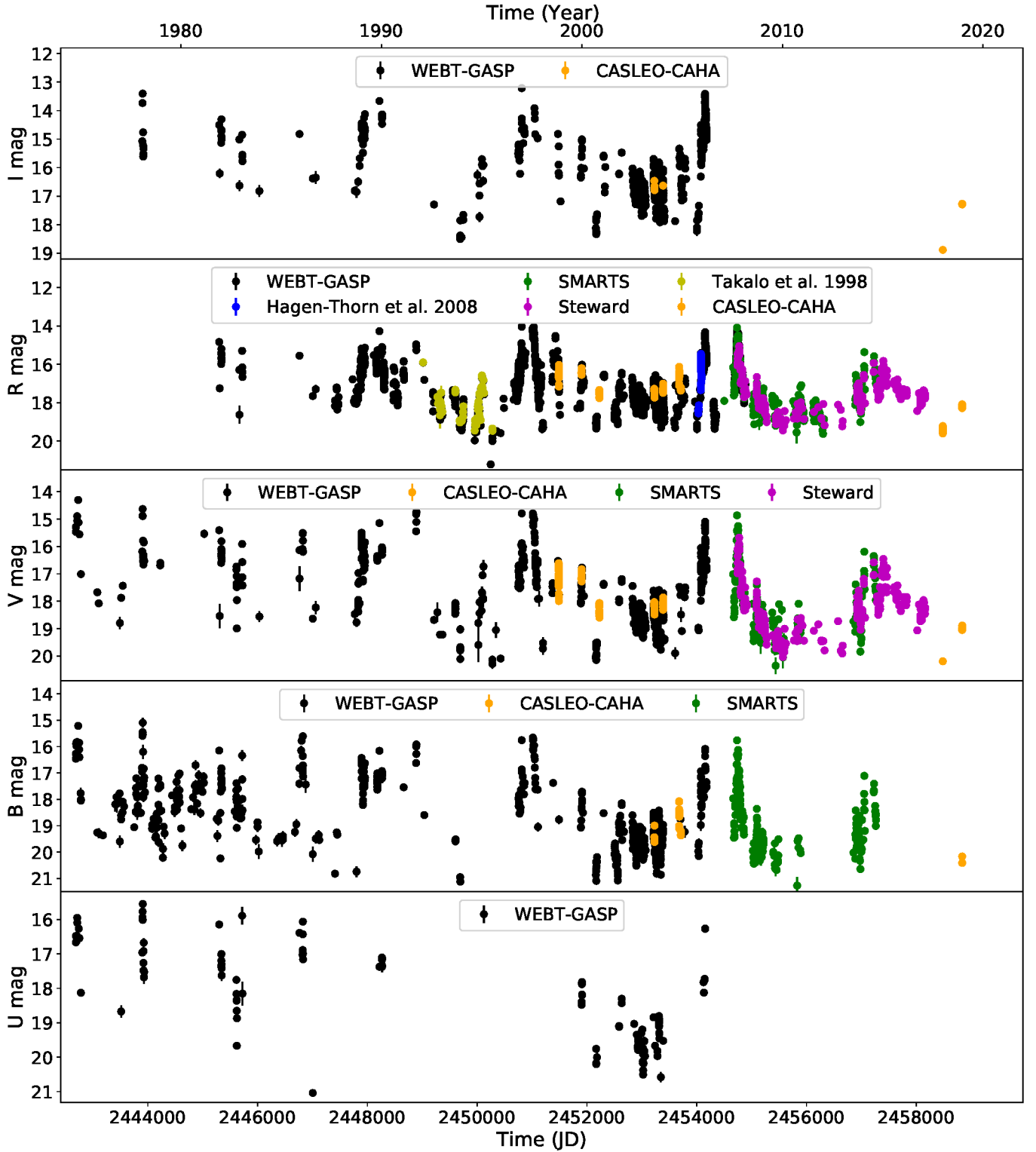
Figure 1. Long-term multiwavelength optical (U, B, V, R, I) lightcurves of AO 0235+164 observed from multiple ground-based telescopes between JD 2442689 (1975 October 3) and JD 2458835 (2019 December 17).

able polarization from radio to optical bands, and emit predominately non-thermal emission in the entire EM spectrum. The low-energy hump is ascribed to synchrotron radiation from relativistic leptons, whereas the high-energy hump arises from inverse Compton (IC) processes and sometimes from hadronic processes (e.g., Marscher 1983; Mücke et al. 2003; Romero et al. 2017, and references therein).

Blazars display flux variability on diverse timescales ranging from a few minutes to several years. Blazar variability has often been divided into three categories, depending on the cadence of the observations: (i) microvariability (Miller et al. 1989), or intraday variability (IDV) (Wagner & Witzel 1995), or intra-night variability (INV) (Sagar et al. 2004), focusing on the variability over a day or less; (ii) short-term variability (STV), focusing on variability over days to weeks, (iii) and long-term variability (LTV), focusing on timescales of months to years (e.g. Gupta et al. 2004).

The BL Lac object AO 0235+164 is at redshift $z = 0.94$ (Cohen et al. 1987). Optical spectroscopic and photometric observations of the object have discovered two foreground-absorbing systems at $z = 0.524$ and $z = 0.851$ (Cohen et al. 1987; Nilsson et al. 1996; Raiteri et al. 2007). The flux of the source can be both absorbed and contaminated by these foreground systems, and the stars in them may act as gravitational microlenses that could contribute to the observed variability. Abraham et al. (1993) did deep CFHT imaging of AO 0235+164 and reported that the source is weakly amplified by macrolensing / microlensing by stars in the foreground.

AO 0235+164 has been extensively observed in the past from radio to γ-ray bands either in individual EM bands or quasi-simultaneously in multiple EM bands and has shown variations in all those bands on diverse timescales (e.g., Madejski et al. 1996; Rabbette et al. 1996; Takalo et al. 1998; Qian et al. 2000; Webb et al. 2000; Romero et al. 2000; Raiteri et al. 2006, 2008; Hagen-Thorn et al. 2008; Gupta et al. 2008; Agudo et al. 2011; Ackermann et al. 2012; Fan et al. 2017; Kutkin et al. 2018; Wang & Jiang 2020, and references therein). It is one of the blazars which has displayed very high and variable optical/NIR polarization up to $\sim$45 percent (e.g., Impey et al. 1982; Stickel et al. 1993; Fan & Lin 1999; Cellone et al. 2007; Ikejiri et al. 2011; Itoh et al. 2016, and references therein). In the Hamburg quasar monitoring program (HQM) this source was observed in the optical R band during 1988–1993, during which a 2.36±0.25

magnitude variation was detected; a particularly strong brightening in the source of $\sim$1.6 magnitude was reported during February 20–22, 1989 (Schramm et al. 1994). In six nights of optical B and V bands observations during 21–27 September 1992, the blazar was found in an unusually bright state and IDV was detected in both B and V bands (Rabbette et al. 1996). On another occasion, 6 nights of quasi-simultaneous V and R band observations in November 1999, revealed IDV with an amplitude of $\sim$100 percent over timescales of a day, while 0.5 magnitude changes were reported in both bands on a single night (Romero et al. 2000). In multicolor optical/NIR photometric ($BVRIJHK$) and R-band optical polarimetric observations of AO 0235+164 during its 2006 December outburst, variability on IDV timescales was detected, with increasing minimum timescale of variability from optical to NIR wavelengths; such variations were even detected in the optical polarization (Hagen-Thorn et al. 2008). In three nights of optical observations of the blazar in January – March 2007, IDV and STV were detected (Gupta et al. 2008).

In quasi-simultaneous optical (V and R bands) and radio (22 GHz) observations of AO 0235+164 during 1993–1996, the variability in optical bands showed amplitudes up to 1.5 magnitudes on STV timescales; although the radio variability is less dramatic, in general, it followed the optical behavior (Takalo et al. 1998). For the 1997 AO 0235+164 outburst, quasi-simultaneous multi-wavelength (MW) (radio, optical, NIR, and X-ray) observations were carried out. It was found that the source varied nearly simultaneously over 6 decades in frequency during the outburst and this result was explained in terms of a microlensing event (Webb et al. 2000).

An analysis of this source's variability over $\sim$25 years led to the suggestion of a $\sim$5.7 years quasi-periodicity of the main radio and optical flares (Raiteri et al. 2001); however, the putative next outburst, predicted to peak around February–March 2004, did not occur, and a new analysis of the optical light curves on a longer time span revealed a characteristic variability timescale of $\sim$8 years, which was also present in the radio data (Raiteri et al. 2006). Recently, optical R band photometric data taken during 1982–2019 showed 5 cycles of double-peaked periodicity of $\sim$8.13 years with a secondary peak following the primary one by $\sim$(1.5–2.0) years (Roy et al. 2022). In another MW campaign from radio to UV bands in 2006–2007, a huge NIR-optical-UV outburst with brightness increase of $\sim$5 magnitudes

during February 19 – 21, 2007 was detected (Raiteri et al. 2008). During a major outburst seen in 2009, changes in radio, optical, X-ray, and γ-ray bands were found to be strongly associated (Agudo et al. 2011). In another simultaneous MW observing campaign of this blazar between 2008 September and 2009 February, γ-ray activity was found to be well correlated with a series of NIR/optical flares, accompanied by an increase in the optical degree of polarization; the X-ray light curve showed a different 20-day high state of an unusually soft spectrum which did not match the extrapolation of the optical/UV synchrotron spectrum (Ackermann et al. 2012).

AO 0235+164 is one of the sources that often used to be called OVV (optically violently variable). There are several such objects, like 3C 279, 3C 454.3, 4C 29.45, CTA 102, BL Lacertae, etc. Long-term achromaticity and zero lags have widely been found for these sources (Bonning et al. 2012; Zhang et al. 2021; Fan et al. 2006; Raiteri et al. 2017; Guo et al. 2015). AO 0235+164 is peculiar because it is commonly considered a BL Lac, one of the furthest known, but it shares properties with FSRQs. It is also a complex source because its light is contaminated by the southern AGN, ELISA, and absorbed by an intervening galaxy. This paper has undertaken a detailed analysis of the source's optical brightness and spectral variability over a very long time span ($\sim$5 decades) as well as an investigation of its central engine. Our aim is to shed light on the long and short-term behavior of an emblematic BL Lac object through a detailed analysis of what is likely the most massive data set ever assembled for an object of this kind. The paper is organized as follows. In section 2, we provide descriptions of the observations of AO 0235+164. The section 3 gives our data analysis methods and results. We present a discussion and conclusions in section 4 and section 5, respectively.

2. OBSERVATIONS

Most of the optical $UBVRI$ observations of AO 0235+164 we have employed in this work are taken from The Whole Earth Blazar Telescope[1] (WEBT) (Villata et al. 2002; Raiteri et al. 2017) which is an international collaboration of optical, near-infrared, and radio observers. WEBT has organized several monitoring campaigns on the blazar AO 0235+164, with the participation of many tens of observers and telescopes all around the world. Later, this source was studied

by the WEBT and by its GLAST-AGILE Support Program (GASP) (Villata et al. 2008, 2009), which was started in 2007 to record quasi-simultaneous data of various blazars observed by the *AGILE* and *Fermi* (formerly *GLAST*) satellites. WEBT/GASP data on AO 0235+164 were published in Raiteri et al. (2001, 2005, 2006, 2008) and Ackermann et al. (2012). Raiteri et al. (2005) prescribed ways to remove the contribution of the southern galaxy ELISA from the observed optical flux densities and estimated the amount of absorption towards the source in excess of that from our Galaxy in X-ray, ultraviolet, optical, and near-infrared bands.

The WEBT and GASP data were calibrated following a common prescription, i.e., with the same photometry for the same reference stars. For calibration of the AO 0235+164 observations, the adopted photometric sequence includes stars 1, 2, and 3 from Smith et al. (1985). To build a reliable lightcurve for further analysis, clear outliers were removed and minor systematic offsets between various datasets were corrected.

AO 0235+164 was also observed with the 2.2 m telescope of Calar Alto Astronomical Observatory (CAHA, Spain) in November – December 2005, using the CAFOS instrument in imaging polarimetry mode, and photometric data were obtained by adding up the ordinary and extraordinary fluxes from each individual image (Cellone et al. 2007). Photometric data were also obtained with the 2.15 m telescope at Complejo Astronómico El Leoncito (CASLEO, Argentina) along several runs in November 1999, December 2000, August 2004, and January 2005. Results from these data were published in Romero et al. (1999, 2000, 2002) and in two papers by the WEBT collaboration focused on this blazar (Raiteri et al. 2005, 2006). Data from a more recent (December 2019) observing run with the same telescope were used in Roy et al. (2022). Magnitude calibration to the standard system was done using our own photometry of Landolt's (2009) fields as well as standard stars in the field of AO 0235+164 (Smith et al. 1985; González-Pérez et al. 2001).

We also collected the publicly available optical R and V-band data of AO 0235+164, taken at Steward Observatory[2], University of Arizona. These measurements employed the 2.3 m Bok and 1.54 m Kuiper telescopes between 4 October 2008 and 12 February 2018, using the SPOL CCD Imaging/Spectropolarimeter attached

---

[1] https://www.oato.inaf.it/blazars/webt

[2] http://james.as.arizona.edu/~psmith/Fermi/DATA/Rphotdata.html

Table 1. Result of flux variability on optical *UBVRI* long-term lightcurves of AO 0235+164

Optical filter	Total Obs.	$\chi^2_{\mathrm{red.}}$	$\chi^2_{0.999,\mathrm{red.}}$	Status	Variability amplitude (%)
U	109	904.5	1.47	V	548.8
B	894	3246.7	1.15	V	590.9
V	1403	5968.4	1.12	V	589.0
R	5675	8715.5	1.06	V	718.8
I	1173	3555.2	1.13	V	567.5

NOTE—In the fourth column 'V/NV' represents variable/non-variable status.

to those two telescopes. Details about the instrument, observation, and data analysis are given in Smith et al. (2009). In addition, we included the optical-*BVR* data from the Small and Moderate Aperture Research Telescope System (SMARTS) public archive[3]. The SMARTS consortium is part of the Cerro Tololo Inter-American Observatory (CTIO), Chile, and has been observing Fermi-Large Area Telescope (LAT)-monitored blazars in the optical *B*, *V*, *R* and NIR *J* and *K* bands. Details about the SMARTS instruments, observations, and data analysis procedures are given in Bonning et al. (2012). These standard magnitudes observed by CASLEO, CAHA, SMARTS, and the Steward observatory were further corrected for the southern galaxy ELISA following Raiteri et al. (2005). We also added other *R*-band optical photometric data from the literature (Takalo et al. 1998; Hagen-Thorn et al. 2008).

3. DATA ANALYSIS METHODS AND RESULTS

We combined all the optical *U*, *B*, *V*, *R*, *I* band data to plot the long term (1974–2020) MW lightcurves of blazar AO 0235+164 (Figure 1). We removed the observations with errors of more than 0.1 magnitudes and studied long-term and intraday variability, color variation, spectral properties, and inter-band correlations.

3.1. *Flux variability studies*

We use different tools on the observed optical magnitudes to quantify the variability timescales and the corresponding significance in multiple optical wavebands.

3.1.1. *The χ^2 test*

For a time series of flux density observations, the χ^2 is defined as,

$$\chi^2 = \sum_{i=1}^{N} \frac{(\mathcal{M}_i - \bar{\mathcal{M}})^2}{\varepsilon_i^2} \qquad (1)$$

where $\mathcal{M}_i$ is the magnitude obtained at the ith observation, ε_i is the corresponding error in measurement, and $\bar{\mathcal{M}}$ is the average magnitude. If the obtained χ^2 value is higher than the critical χ^2 value at 99.9 per cent significance level, we consider the source as variable. The critical value ($\chi^2_{0.999,d}$) depends on the degrees of freedom (d) of the dataset. The reduced χ^2 values listed in Table 1 indicate that the source exhibits significant flux variations in all the optical wavebands.

3.1.2. *Variability amplitude*

According to the relation given by Heidt & Wagner (1996), we estimated the variability amplitudes (V_M) in percentage for the lightcurves in different wavelengths using the following formula,

$$V_M = 100 \times \sqrt{(\mathcal{M}_{\mathrm{max}} - \mathcal{M}_{\mathrm{min}})^2 - 2\,\bar{\varepsilon}^2}\ (\%) \qquad (2)$$

where $\mathcal{M}_{\mathrm{max}}$ and $\mathcal{M}_{\mathrm{min}}$ are the maximum and minimum observed magnitude in a lightcurve, respectively, while $\bar{\varepsilon}$ is the average error in magnitude measurements. We list the calculated variability of amplitudes in Table 1.

3.1.3. *Correlation study*

To study the inter-band correlations, we first generated 15-minute binned optical *UBVRI* lightcurves, and plotted the average *U*, *B*, *V*, and *I*-magnitudes against the average *R*-magnitudes for the time bins when the source was observed at both the wavebands (Figure 2). The magnitude-vs-magnitude plots show very good linear correlations. To take the uncertainty of magnitude measurements into account, we simulated 10000 datasets assuming that each magnitude measurement is Gaussian distributed. Then we calculated the mean and standard deviation of the Pearson correlation coefficients of all simulated datasets. We obtained high correlations (> 0.9) with small uncertainties (< 0.003) between all wavebands.

Moreover, to find any time lag between the correlated optical lightcurves we computed the discrete correlation function (DCF) from the unbinned multiwavelength light curves, as the light curves consist of discrete data points. Following the method of Edelson & Krolik (1988), we computed the unbinned DCF (UDCF) be-
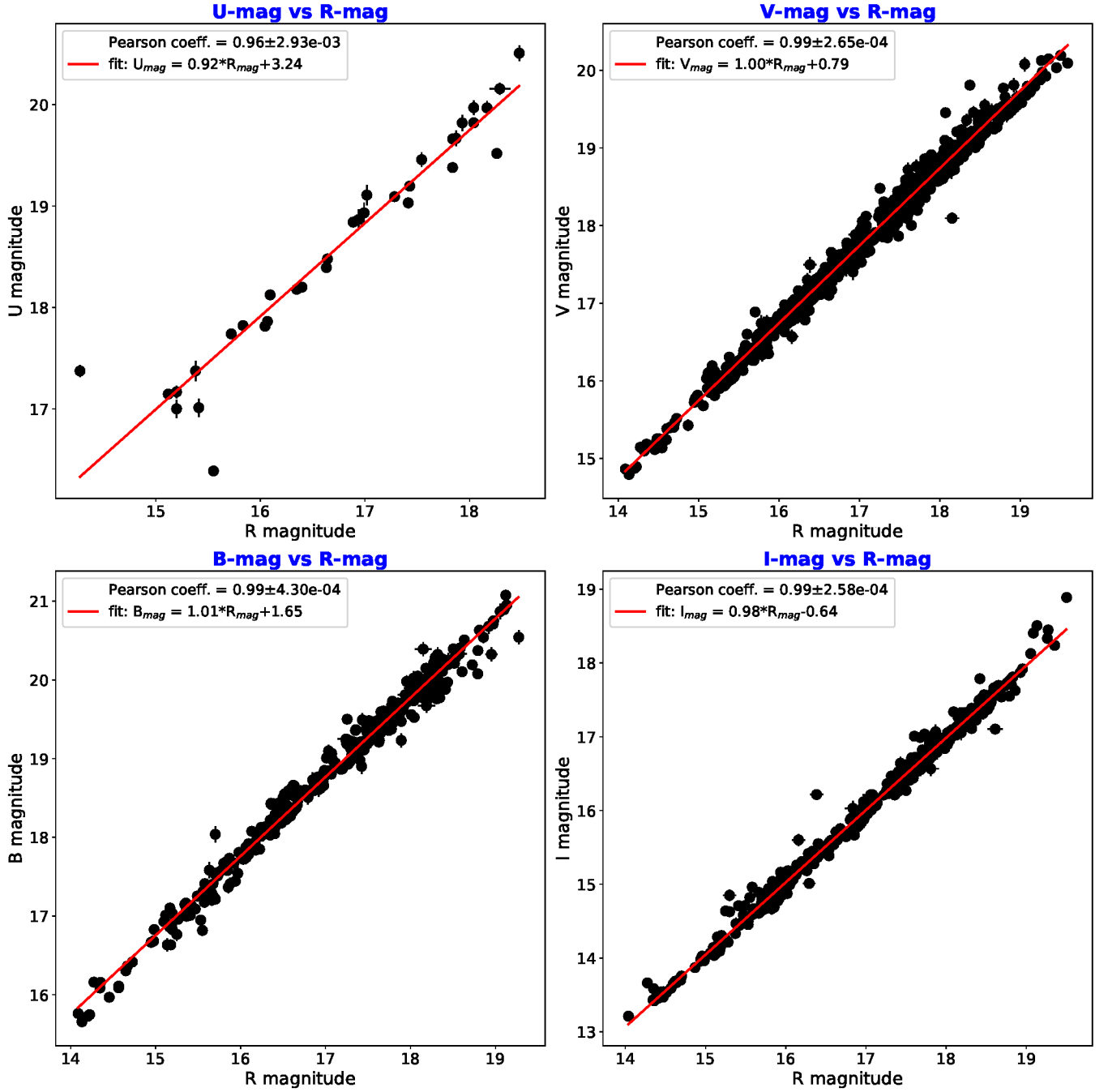
Figure 2. 15-minute averaged $UBVI$ magnitudes versus R-magnitude plots for correlation study. U, B, V, and I-band observations show high linear correlation with R-band data. All the plots are fitted with straight lines.

tween the ith data point in one waveband (a) and the jth data point in another (b) as

$$\text{UDCF}_{ij} = \frac{(a_i - \bar{a})(b_j - \bar{b})}{\sigma_a \sigma_b}, \qquad (3)$$

where $\bar{a}$ and $\bar{b}$ are the mean of the observed magnitudes, and σ_a and σ_b are the standard deviations of the corresponding datasets. Next, we calculated the discrete

correlation function (DCF) at a certain time lag τ by averaging the UDCF_{ij}s whose corresponding time lags $\Delta t_{ij} = t_i^a - t_j^b$ lie within the range $[\tau - \frac{\Delta \tau}{2}, \tau + \frac{\Delta \tau}{2}]$ ($\Delta \tau$ is the time lag bin width), such that,

$$\text{DCF}(\tau) = \frac{1}{n} \sum \text{UDCF}_{ij}(\tau). \qquad (4)$$

Following the suggestion of White & Peterson (1994), we computed the mean magnitudes ($\bar{a}$ and $\bar{b}$) and the
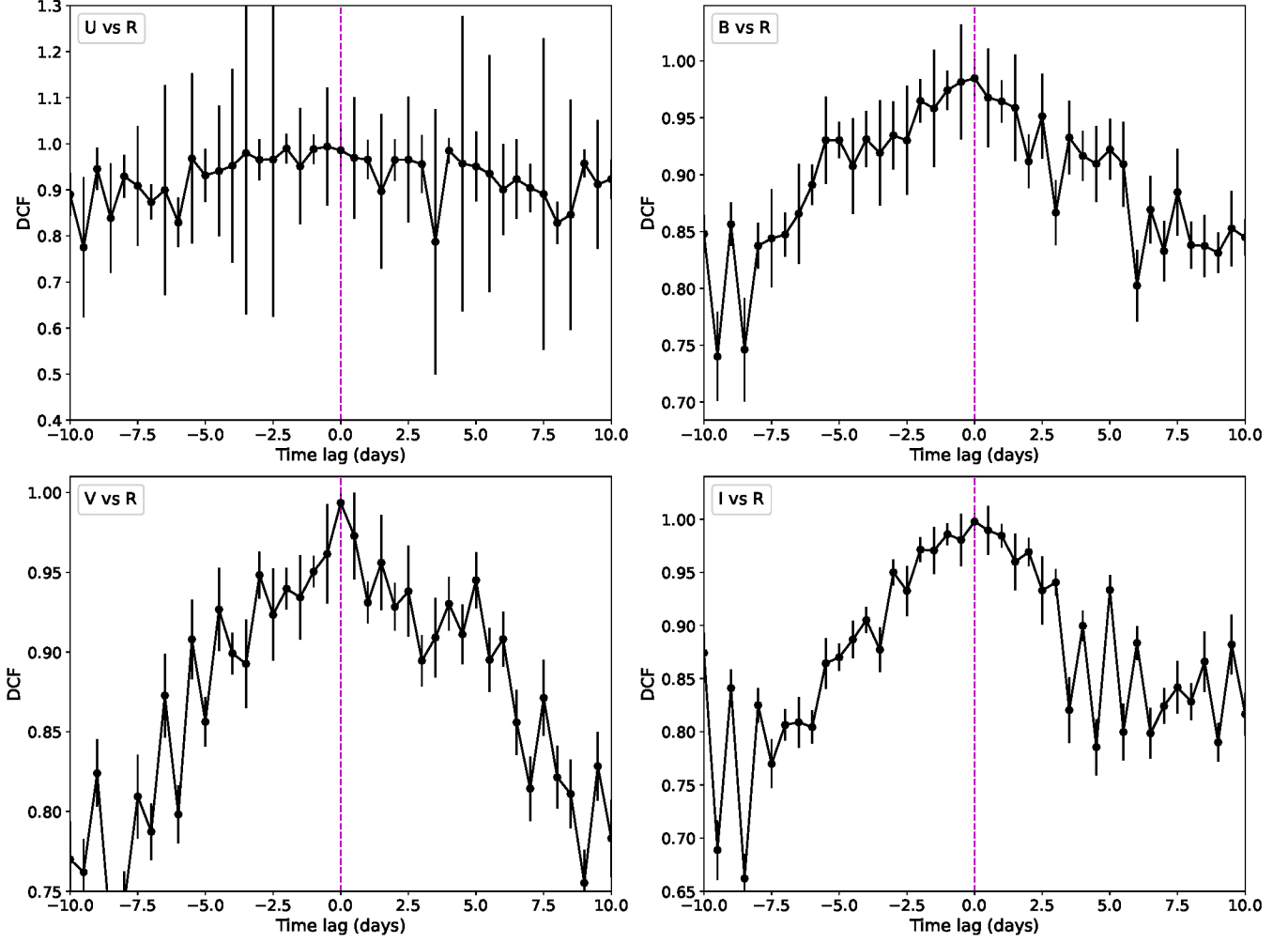
Figure 3. Results of discrete cross-correlation analysis of U, B, V, and I-band with respect to R-band in the full time range.

standard deviations (σ_a and σ_b) in Equation 3 using only those data points who fall within a given time lag bin, as the mean and standard deviation keep on changing for a time series originated from a stochastic process such as blazar emission. The error in the DCF(τ) computation in each bin is calculated as

$$\sigma_{\mathrm{DCF}}(\tau) = \frac{1}{M-1}\sqrt{\sum_{k=1}^{M}(\mathrm{UDCF}_k - \mathrm{DCF}(\tau))^2}. \quad (5)$$

Figure 3 shows the DCFs of $UBVI$ bands with respect to the R-band observations. In all cases, the DCFs peak at zero time lag, except the U-band vs R-band DCF due to poor data sampling in the U-band. This explains the strong linearity in Figure 2 and implies that the emission at all optical wavebands are coming from the same region in the jet and are produced from the same radiation mechanism.
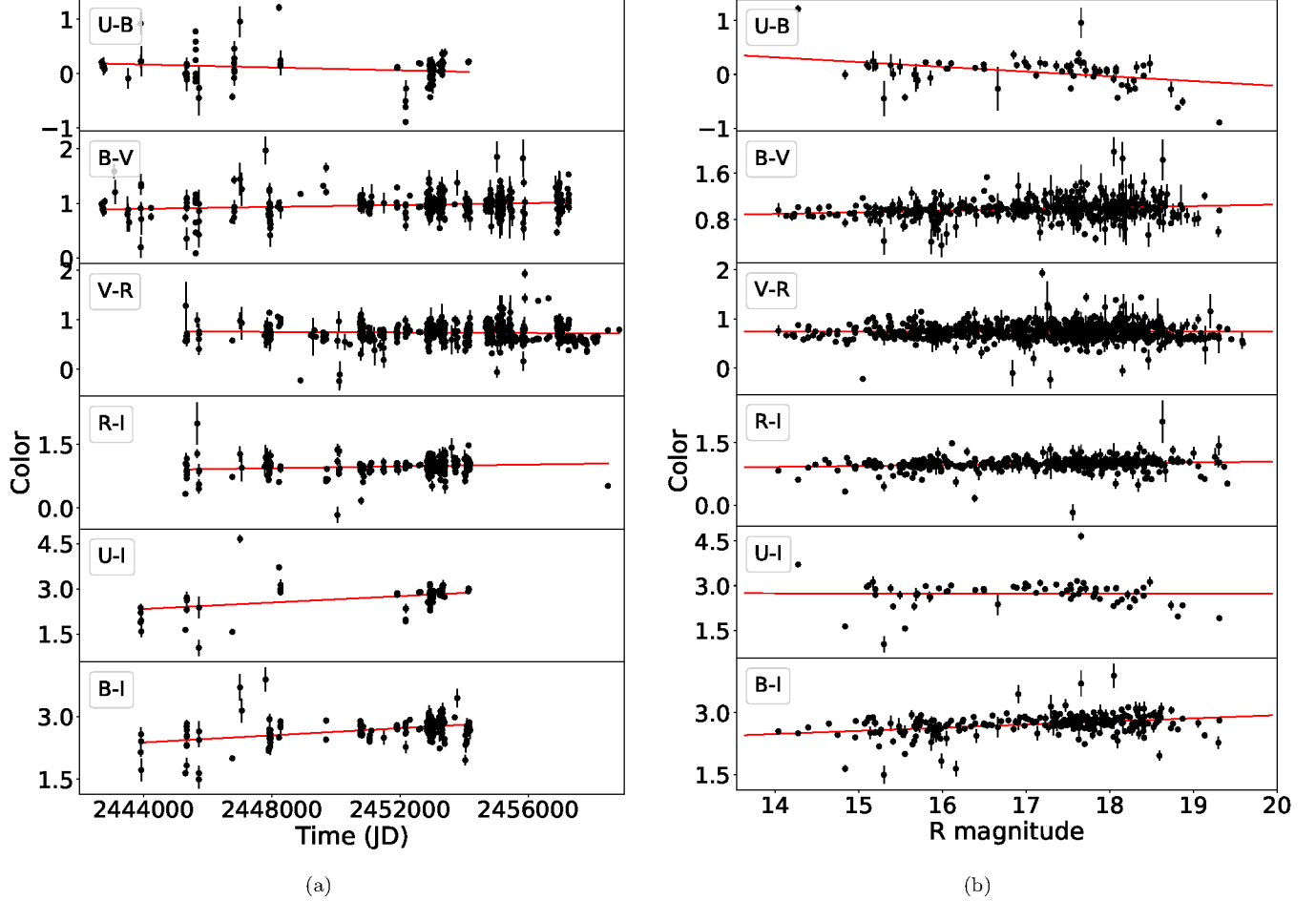
Table 2. Color variation with time in optical $UBVRI$ long-term lightcurves of AO 0235+164

CI	m	c	ρ	p
$U-B$	-1.52E-05	3.74E$+01$	-2.06E-01	8.28E-02
$B-V$	6.58E-06	-1.52E$+01$	1.42E-01	4.79E-03
$V-R$	-5.34E-06	1.38E$+01$	-9.19E-02	1.39E-02
$R-I$	1.83E-05	-4.40E$+01$	2.85E-01	1.74E-08
$U-I$	5.63E-05	-1.35E$+02$	4.03E-01	1.88E-03
$B-I$	4.16E-05	-9.92E$+01$	4.50E-01	3.41E-11

NOTE—In the column headings: CI: color indices; m = slope; c = intercept; ρ = Pearson coefficient; p = null hypothesis probability for Figure 4a

3.1.4. Color Variations

The term 'color' denotes the magnitude difference between two quasi-simultaneous observations at two dif-

(a)   (b)

Figure 4. (a) Color variation with time. (b) Color variation with optical R magnitude. The red line in each panel represents the straight line fit. Fit parameters are given in Table 2 and Table 3 respectively.

Table 3. Color variation with R-band magnitude in optical $UBVRI$ long-term lightcurves of AO 0235+164

CI	m	c	ρ	p
$U-B$	-1.36E-01	2.37E$+00$	-5.37E-01	3.35E-05
$B-V$	1.62E-02	7.04E-01	1.41E-01	7.41E-03
$V-R$	-3.54E-03	7.98E-01	-2.58E-02	4.92E-01
$R-I$	1.62E-02	7.00E-01	1.37E-01	7.59E-03
$U-I$	-6.47E-02	3.85E$+00$	-2.07E-01	1.30E-01
$B-I$	6.23E-02	1.66E$+00$	3.66E-01	1.69E-07

NOTE—In the column headings: CI: color indices; m = slope; c = intercept; ρ = Pearson coefficient; p = null hypothesis probability for Figure 4b

ferent wavebands. We plotted the variation of optical colors ($U-B$, $B-V$, $V-R$, $R-I$, and $B-I$) with time and R-magnitude in Figure 4. We listed the re-

sults of a straight line ($Y = mX + c$) fitting to all these plots in Table 2 and Table 3. The linear fits of the color versus time plots do not show any trend, except for the rather sparsely sampled ($B-I$) color, which has a high slope (4.16×10^{-5}) in Figure 4a, along with the highest Pearson correlation coefficient (0.45), and the lowest null hypothesis probability (3.41×10^{-11}). Among the color versus magnitude relations, the strongest relationship is between ($B-I$) and R (Figure 4b), having a positive slope (6.23×10^{-2}) with the highest Pearson coefficient (0.37) and the lowest p-value (1.69×10^{-7}) (Table 3), indicates a bluer-when-brighter (BWB) trend when the widest range of the available colors is considered.

3.1.5. *Spectral Variations and SEDs*

We plotted the optical (BVR) spectral energy distributions for the nights where observations were taken at all of these three filters. Following the prescription of Raiteri et al. (2005), we took into account the total absorption by the Milky Way galaxy and the foreground
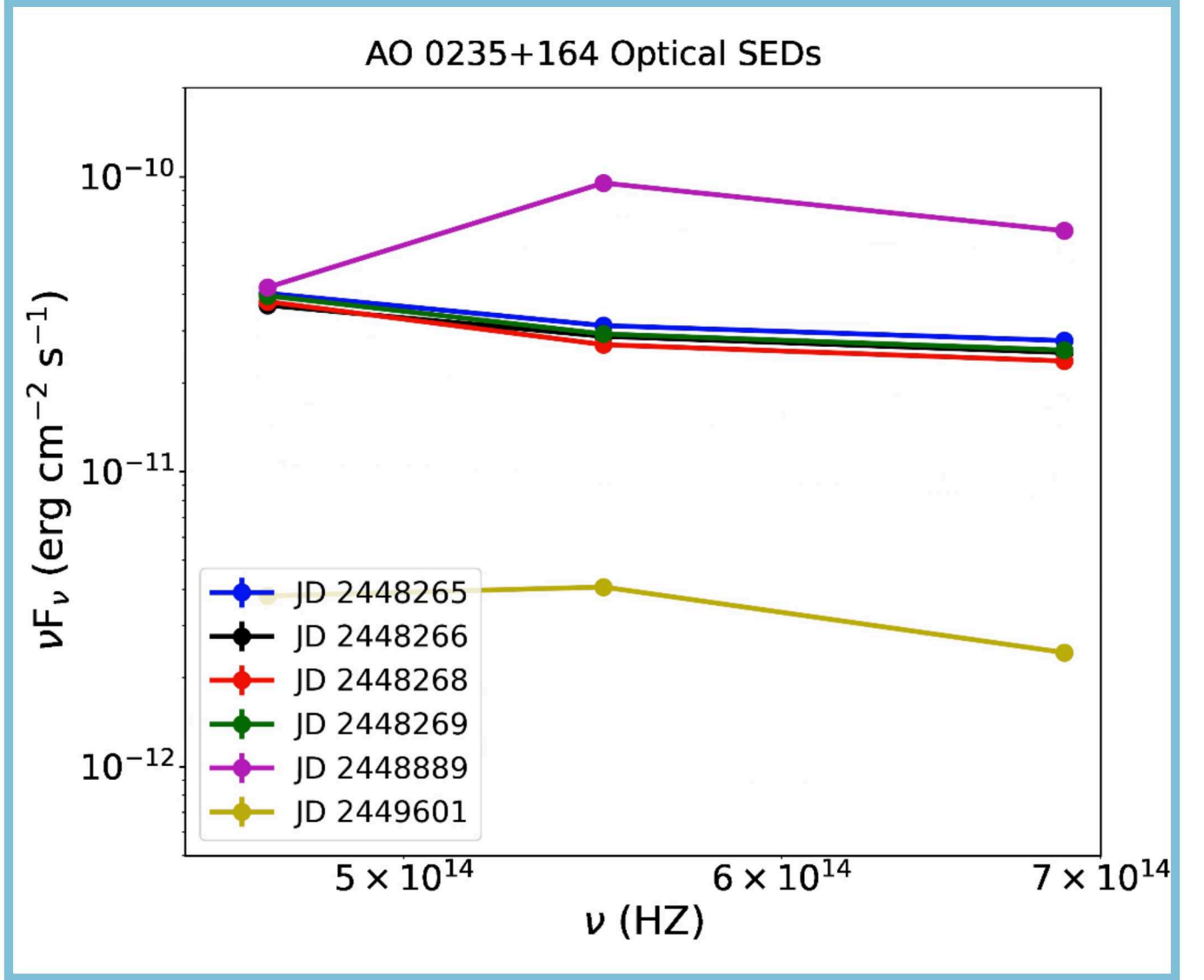
Figure 5. An example frame of the AO 0235+164 optical SED animation that is available in the HTML version of this article. The duration of the animation is 1 minute and it contains a total of 360 one-day averaged optical SEDs, having 6 SEDs per frame. The observation dates of the SEDs are given in the plot legend.

Table 4. Spetral index variation with R-band magnitude and time in optical $UBVRI$ long-term lightcurves of AO 0235+164
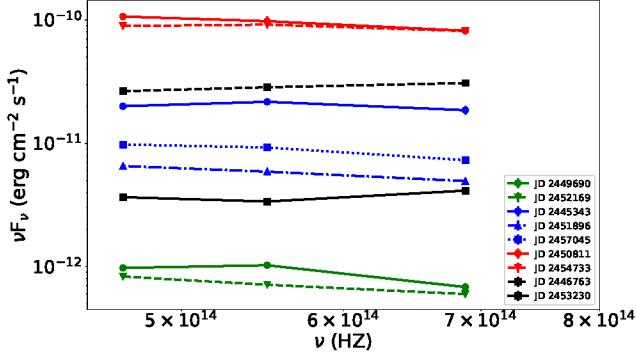
Dependency	m	c	ρ	p
α_{VR} vs R	-2.01E-02	3.30E+00	-2.58E-02	4.92E-01
α_{VR} vs JD	-3.03E-05	7.74E+01	-9.19E-02	1.39E-02

NOTE—In the column headings: m = slope; c = intercept; ρ = Pearson coefficient; p = null hypothesis probability for Figure 7.

tudes of respective wavebands and then converted them into extinction-corrected flux densities, F_ν. The accompanying video contains one-day averaged optical SEDs for those 360 nights (An example frame is shown in Figure 5). Figure 6 shows a few examples of SEDs of low, moderate, and high flux states, plotted in $(\nu F_\nu - \nu)$ format. Mostly, the SEDs have a declining shape following a power law. However, there are evidences of spectral hardening on several nights (e.g., JD 2445337, JD 2445721, JD 2448889, JD 2452901, JD 2453230).

From the one-day binned multiwavelength lightcurves we calculated the spectral indices (α_{VR}) for all the days when the source was observed in both V and R bands,

absorber at $z = 0.524$, and subtracted the extinction magnitudes ($A_U = 2.519$, $A_B = 1.904$, $A_V = 1.473$, $A_R = 1.260$, $A_I = 0.902$) from the calibrated magni-

Figure 6. Examples of AO 0235+164 optical intraday SEDs during three different states of brightness: (i) the green lines represent SED during quiescent states (νF_ν (erg cm^{-2} s^{-1}) $< 10^{-12}$), (ii) the blue lines show SED during moderately bright states ($10^{-12} < \nu F_\nu$ (erg cm^{-2} s^{-1}) $< 3\times10^{-11}$), (iii) the red lines show SED during outbursts (νF_ν (erg cm^{-2} s^{-1}) $> 5\times10^{-11}$). The black lines are examples of SED with spectral hardening on JD 2446763 and JD 2453230.

using the formula given by Wierzcholska et al. (2015) on extinction corrected magnitudes, as

$$\alpha_{VR} = \frac{0.4(V - R)}{\log(\nu_V/\nu_R)}, \qquad (6)$$

where ν_V and ν_R respectively represent the effective frequencies of V and R band filters (Bessell 2005). We plotted the variation of spectral indices with time and R-band magnitude (Figure 7) and listed the results of linear fits, Pearson coefficient, and null hypothesis probability in Table 4. We do not find any significant long-term variation of the spectral index with time, nor is there a correlation with R-magnitude.

3.2. *Intraday Variability*

We applied four frequently used statistical tests for IDV: scaled C-criterion, scaled F-test, the power-enhanced F-test, and the nested analysis of variance (ANOVA) test (de Diego 2014; de Diego et al. 2015; Zibecchi et al. 2017, 2020) to detect statistically significant intraday flux variability in AO 0235+164 lightcurves observed by CASLEO and CAHA telescopes. These tests mainly compare the variations in blazar magnitudes with the variations in magnitudes of one or more stars within the field-of-view of the blazar and have different advantages and disadvantages. We collected data from multiple field stars along with the blazar data (Table 5). We applied the first three methods on the intraday differential lightcurves of AO 0235+164 where at least 10 observations were recorded per night with at least one optical filter between 1999 November 2 to 2019 December 17. We employed the nested ANOVA test only on lightcurves having at least 20 observations per night.

Table 5. Equivalence between internal field star numbering in the CASLEO/CAHA data used in the IDV analyses and field-star numbering in other standard star charts during different observation seasons

Season	CASLEO/CAHA	Heidelberg[a]	GKM2001[b]
1999–2001	2	8	10
(CASLEO)	4	C1	9
	5	6	11
	7	–	1
	8	–	3
	10	–	8
	12	–	16
2004–2005	2	8	10
(CASLEO)	4	C1	9
	5	6	11
	6	–	8
	7	–	7
2005	2	8	10
(CAHA)	11	C1	9
	12	–	1
	13	–	3
	14	–	7
	15	–	8
	16	6	11
	17	–	16
2018–2019	2	8	10
(CASLEO)	4	C1	9
	5	6	11
	6	–	8
	7	–	7
	8	–	16

NOTE—*a*.   https://www.lsw.uni-heidelberg.de/projects/extragalactic/charts/0235+164.html
*b*. González-Pérez et al. (2001)

3.2.1. *Scaled C-criterion*

Differential photometry, where the blazar magnitudes are compared to one or more stars in the same field of view, is the usual technique for obtaining blazar lightcurves free from the effects of any non-astrophysical fluctuations. The simplest differential photometry involves a single comparison star, while a second star, whose magnitudes are measured against the same comparison star, is used for a stability check. We denote B, S1, and S2 as the blazar, comparison, and control star, respectively. The variability test requires two differential lightcurves (DLC): (blazar–comparison star) and (control star–comparison star). The latter is believed

Table 6. Result of scaled C-criterion and F-test for IDV on AO 0235+164 differential lightcurves from CASLEO and CAHA

Date	JD	Band	No. of obs.	S1, S2	Γ	C_Γ	F_Γ	$F_c^{0.005}$	Status	Final Status
1999 Nov 2	2451485	V	23	2,3	0.8886	11.3640	129.1405	3.1246	V	V
				2,6	1.0867	12.9184	166.8856	3.1912	V	
				2,10	1.6876	8.1627	66.6298	3.1246	V	
				2,11	0.7431	13.4002	179.5650	3.1246	V	
1999 Nov 3	2451486	V	22	2,3	1.0707	5.6976	32.4624	3.1347	V	V
				2,11	0.8841	6.0726	36.8768	3.1347	V	
1999 Nov 4	2451487	R	30	2,3	1.0059	8.4058	70.6582	2.6737	V	V
				2,11	0.6639	9.8857	97.7278	2.6737	V	
		V	30	2,3	0.9994	8.9281	79.7104	2.6737	V	V
				2,11	0.8286	9.6683	93.4770	2.6737	V	
1999 Nov 5	2451488	R	23	2,3	1.4994	1.5631	2.4433	3.1246	NV	NV
				2,11	0.9852	1.9303	3.7260	3.1246	NV	
		V	22	2,3	1.4403	3.0342	9.2064	3.1347	V	V
1999 Nov 6	2451489	R	30	2,3	0.8471	17.5775	308.9682	2.6737	V	V
				2,6	0.9769	12.3281	151.9824	2.6737	V	
				2,7	1.3573	9.9373	98.7501	2.7048	V	
				2,8	1.3805	9.8381	96.7876	2.7048	V	
				2,10	1.6936	6.8657	47.1376	2.6737	V	
				2,11	0.5616	15.4338	238.2019	2.6737	V	
		V	29	2,3	0.8485	18.1892	330.8486	2.7233	V	V
				2,6	1.0013	11.7527	138.1254	2.7233	V	
				2,7	1.3527	12.5480	157.4516	2.7397	V	
				2,8	1.4133	13.4172	180.0214	2.7397	V	
				2,10	1.5626	17.6674	312.1376	2.7233	V	
				2,11	0.7018	17.9948	323.8145	2.7233	V	
1999 Nov 7	2451490	R	11	2,3	0.9562	3.5930	12.9095	5.8479	V	PV
				2,4	1.9798	2.2801	5.1990	5.8479	NV	
				2,6	1.1143	4.3903	19.2751	5.8479	V	
				2,10	1.9703	1.7073	2.9148	5.8479	NV	
				2,11	0.6197	2.9496	8.7003	5.8479	V	
		V	12	2,3	0.9382	2.9304	8.5871	5.3191	V	PV
				2,4	1.7807	1.9342	3.7410	5.3191	NV	
				2,6	1.1169	2.8931	8.3701	5.3191	V	
				2,10	1.7653	2.1046	4.4292	5.3191	NV	
				2,11	0.7772	4.3359	18.7997	5.3191	V	

NOTE—S1 and S2 are the comparison and control star numbers, respectively, used for the IDV tests. Star numbers follow the star maps shown in Table 5.

(a)

(b)
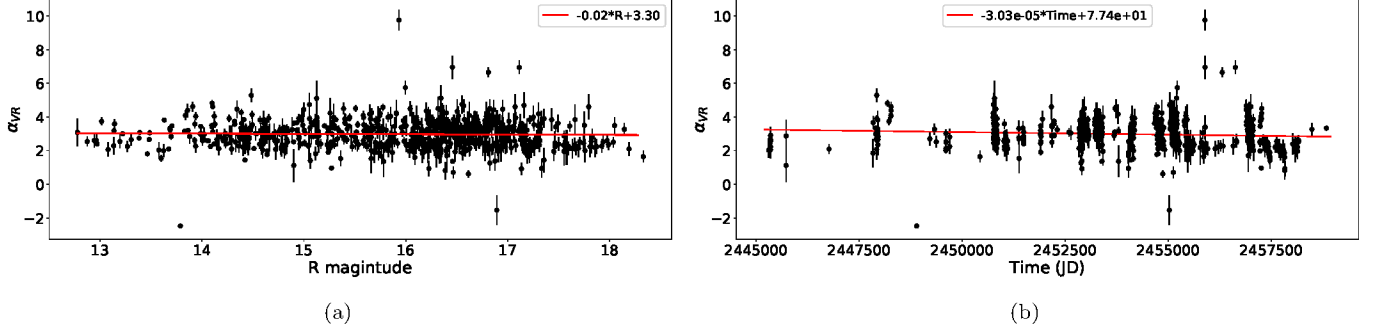
Figure 7. (a) Variation of spectral index (α_{VR}) with R-band magnitude. (b) Variation of α_{VR} with time. The red line at each panel represents the linear fit.

Table 6. Result of scaled C-test and F-test for IDV on AO 0235+164 differential lightcurves from CASLEO and CAHA (continued...)

Date	JD	Band	No. of obs.	S1, S2	Γ	C_Γ	F_Γ	$F_c^{0.005}$	Status	Final status
2000 Dec 21	2451900	R	10	2,3	0.9446	2.3638	5.5876	6.5402	NV	PV
				2,6	1.0793	4.9877	24.8767	6.5402	V	
				2,7	1.5020	2.0187	4.0753	6.5402	NV	
				2,8	1.5289	1.9985	3.9939	6.5402	NV	
				2,9	0.8790	2.5120	6.3100	6.5402	NV	
				2,11	0.6246	7.4168	55.0085	6.5402	V	
		V	10	2,3	0.9509	3.4671	12.0208	6.5402	V	PV
				2,6	1.1202	2.4789	6.1449	6.5402	NV	
				2,7	1.5357	1.8729	3.5079	6.5402	NV	
				2,8	1.6064	2.0031	4.0124	6.5402	NV	
				2,9	1.0966	3.7299	13.9120	6.5402	V	
				2,11	0.7842	1.5920	2.5343	6.5402	NV	
2000 Dec 23	2451902	R	10	2,3	0.8588	4.4475	19.7803	6.5402	V	V
				2,6	0.9890	5.1629	26.6559	6.5402	V	
				2,7	1.3855	3.5919	12.9020	6.5402	V	
				2,8	1.4091	2.8222	7.9646	6.5402	V	
				2,9	0.8000	4.6739	21.8451	6.5402	V	
				2,11	0.5664	5.3690	28.8267	6.5402	V	
				2,13	1.7083	3.0181	9.1089	6.5402	V	
		V	11	2,3	0.8509	6.5241	42.5634	5.8479	V	PV
				2,6	1.0031	5.4277	29.4602	5.8479	V	
				2,7	1.3714	5.0139	25.1395	5.8479	V	
				2,8	1.4341	5.2879	27.9619	5.8479	V	
				2,9	0.9797	1.4805	2.1919	5.8479	NV	
				2,11	0.7013	5.1765	26.7965	5.8479	V	
				2,13	1.5668	4.3770	19.1586	5.8479	V	

NOTE—S1 and S2 are the comparison and control star numbers respectively used for the IDV tests. Star numbers follow the star maps shown in Table 5.
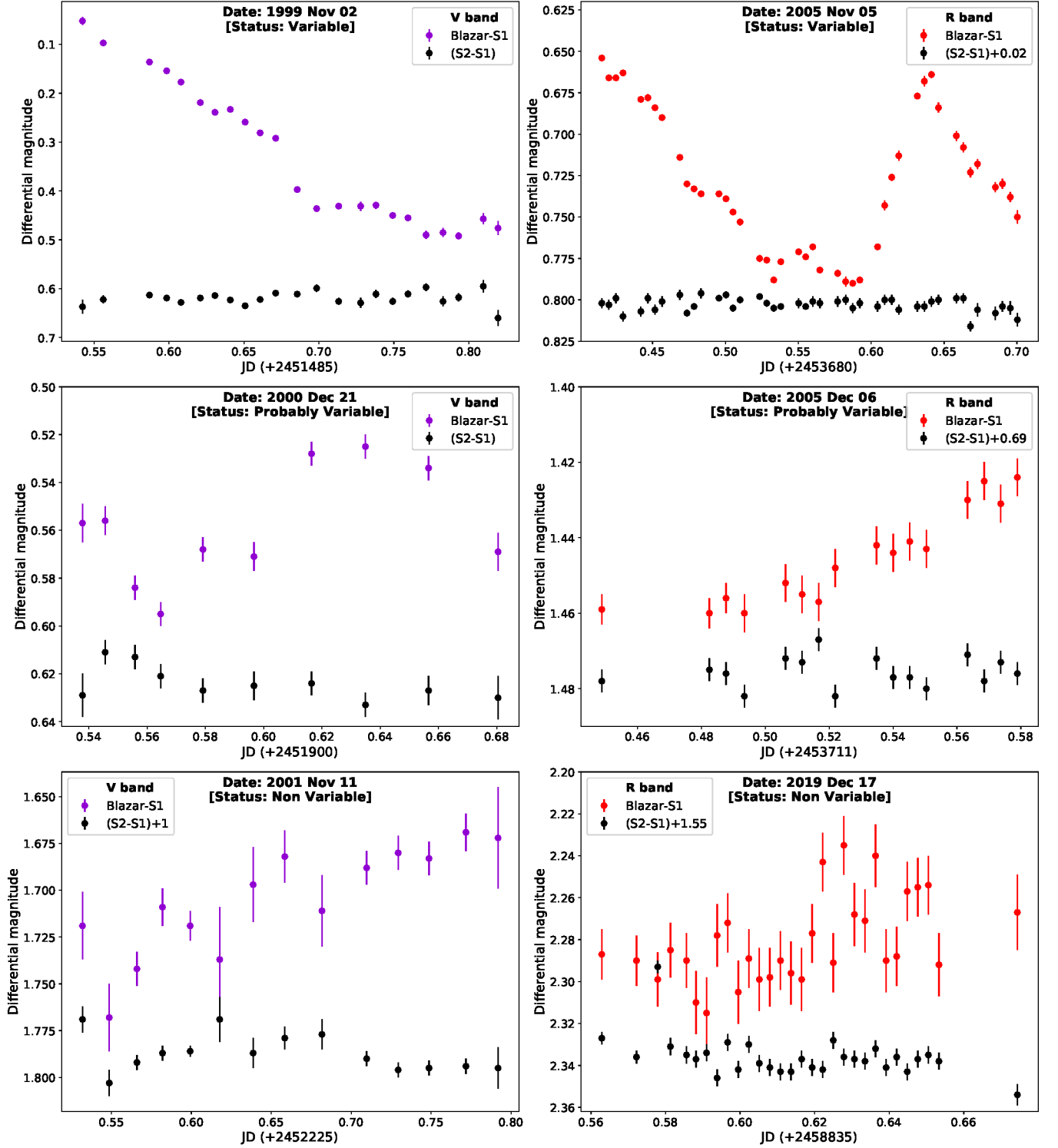
Figure 8. Some intraday lightcurves of AO 0235+164 on nights when the source showed different states of variability. S1 and S2 represent the comparison and control star respectively. In some panels, the differential lightcurve of the control star is shifted to bring it into the same frame of the blazar DLC for better visual comparison of variability.

ROY ET AL.

Table 6. Result of scaled C-test and F-test for IDV on AO 0235+164 differential lightcurves from CASLEO and CAHA (continued...)

Date	JD	Band	No. of obs.	S1, S2	Γ	C_Γ	F_Γ	$F_c^{0.005}$	Status	Final status
2001 Nov 9	2452223	R	12	2,11	1.2042	4.6476	21.5998	5.3191	V	V
		V	12	2,3	1.8778	2.5035	6.2675	5.3191	NV	NV
				2,4	3.6191	1.1450	1.3111	5.3191	NV	
				2,9	2.2039	1.2380	1.5326	5.4171	NV	
				2,10	3.5871	2.0056	4.0226	5.3191	NV	
				2,11	1.5366	1.7566	3.0857	5.3191	NV	
2001 Nov 10	2452224	R	10	2,3	2.3728	1.0570	1.1172	6.5402	NV	NV
				2,9	2.2429	1.1058	1.2229	6.5402	NV	
				2,11	1.5595	0.9395	0.8826	6.5402	NV	
		V	10	2,3	2.3876	1.0788	1.1637	6.5402	NV	NV
				2,9	2.7847	1.3860	1.9209	6.5402	NV	
				2,11	1.9713	0.9038	0.8168	6.5402	NV	
2001 Nov 11	2452225	R	14	2,3	2.0291	1.4125	1.9951	4.5724	NV	NV
				2,9	1.5447	1.2505	1.5638	4.6425	NV	
				2,11	1.3171	1.6860	2.8427	4.5724	NV	
		V	14	2,3	2.0291	1.4125	1.9951	4.5724	NV	NV
				2,9	1.5447	1.2505	1.5638	4.6425	NV	
				2,11	1.3171	1.6860	2.8427	4.5724	NV	
2001 Nov 12	2452226	R	12	2,3	1.8479	1.5819	2.5025	5.3191	NV	PV
				2,11	1.2074	3.0203	9.1222	5.3191	V	
		V	12	2,3	1.8704	1.9230	3.6980	5.3191	NV	NV
				2,4	3.5981	1.0281	1.0571	5.3191	NV	
				2,10	3.5672	2.3374	5.4634	5.3191	NV	
				2,11	1.5330	1.5642	2.4468	5.3191	NV	
2001 Nov 13	2452227	R	11	3,4	2.0213	1.1434	1.3073	5.8479	NV	NV
		V	11	3,4	1.1840	0.6858	0.4703	5.8479	NV	NV

NOTE—S1 and S2 are the comparison and control star numbers respectively used for the IDV tests. Star numbers follow the star maps shown in Table 5.

Table 6. Result of scaled C-test and F-test for IDV on AO 0235+164 differential lightcurves from CASLEO and CAHA (continued...)

Date	JD	Band	No. of obs.	S1, S2	Γ	C_Γ	F_Γ	$F_c^{0.005}$	Status	Final status
2005 Jan 16	2453387	R	11	2,3	1.5238	3.8074	14.4962	5.8479	V	V
				2,4	3.3465	2.7388	7.5010	5.8479	V	
				2,6	3.3316	2.7442	7.5308	5.8479	V	
				2,7	1.4051	3.4058	11.5996	5.8479	V	
2005 Nov 2	2453677	R	32	2,3	1.2848	6.4237	41.2636	2.5846	V	V
				2,4	0.8959	4.5227	20.4545	2.5846	V	
				2,5	0.2571	4.3013	18.5013	2.5846	V	
				2,6	0.5453	3.9310	15.4528	2.5846	V	
				2,7	0.5844	4.9283	24.2884	2.5846	V	
				2,8	0.4738	7.0560	49.7865	2.5846	V	
				2,9	0.3415	6.5374	42.7373	2.5846	V	
				2,10	0.3397	4.0828	16.6695	2.5846	V	
2005 Nov 4	2453679	R	12	2,3	0.8534	4.3059	18.5409	5.3191	V	V
				2,4	0.5599	3.7978	14.4235	5.3191	V	
				2,5	0.1421	5.0805	25.8111	5.3191	V	
				2,6	0.3029	5.3341	28.4524	5.3191	V	
				2,7	0.3534	7.6846	59.0525	5.3191	V	
				2,8	0.2839	4.3153	18.6220	5.3191	V	
				2,9	0.1914	11.0664	122.4647	5.3191	V	
				2,10	0.1875	5.4019	29.1804	5.3191	V	
2005 Nov 5	2453680	R	44	2,3	0.9749	10.6766	113.9894	2.2266	V	V
				2,4	0.6398	9.3431	87.2939	2.2266	V	
				2,5	0.1942	11.0439	121.9674	2.2266	V	
				2,6	0.3721	10.7338	115.2142	2.2266	V	
				2,7	0.4059	10.2100	104.2433	2.2266	V	
				2,8	0.3427	8.3494	69.7127	2.2266	V	
				2,9	0.2399	12.1459	147.5239	2.2266	V	
				2,10	0.2340	8.5775	73.5744	2.2341	V	
2005 Nov 6	2453681	R	40	2,3	1.0022	7.8517	61.6495	2.3212	V	V
				2,4	0.6946	8.8524	78.3645	2.3212	V	
				2,5	0.2051	6.6830	44.6620	2.3212	V	
				2,6	0.4022	7.6630	58.7211	2.3212	V	
				2,8	0.3694	5.9489	35.3890	2.3212	V	
				2,9	0.2576	6.8684	47.1751	2.3212	V	
				2,10	0.2563	5.1520	26.5433	2.3212	V	

NOTE—S1 and S2 are the comparison and control star numbers respectively used for the IDV tests. Star numbers follow the star maps shown in Table 5.

Table 6. Result of scaled C-test and F-test for IDV on AO 0235+164 differential lightcurves from CASLEO and CAHA (continued...)

Date	JD	Band	No. of obs.	S1, S2	Γ	C_Γ	F_Γ	$F_c^{0.005}$	Status	Final status
2005 Nov 8	2453683	R	28	2,3	0.9329	2.4256	5.8834	2.7940	NV	NV
				2,4	0.6336	2.3363	5.4585	2.7770	NV	
				2,5	0.1788	1.7843	3.1836	2.7770	NV	
				2,6	0.3598	2.2163	4.9120	2.7770	NV	
				2,7	0.4059	1.4945	2.2335	2.7770	NV	
				2,8	0.3451	2.1606	4.6682	2.9002	NV	
				2,9	0.2318	1.3895	1.9307	2.7770	NV	
2005 Dec 5	2453710	R	20	2,3	1.4796	1.4053	1.9748	3.4317	NV	NV
				2,4	1.0247	0.7240	0.5242	3.4317	NV	
				2,5	0.3133	0.9355	0.8752	3.4317	NV	
				2,6	0.6030	1.1896	1.4151	3.4317	NV	
				2,8	0.5634	1.0332	1.0674	3.4317	NV	
				2,9	0.3979	1.0716	1.1482	3.4317	NV	
				2,10	0.3915	0.8994	0.8089	3.4317	NV	
2005 Dec 6	2453711	R	16	2,3	1.4092	2.1709	4.7129	4.0698	NV	PV
				2,4	0.9785	3.7432	14.0118	4.0698	V	
				2,5	0.2848	2.1323	4.5467	4.0698	NV	
				2,6	0.5570	2.7562	7.5967	4.0698	V	
				2,7	0.6157	1.8489	3.4186	4.0698	NV	
				2,8	0.5266	1.3717	1.8815	4.0698	NV	
				2,8	0.5266	1.3717	1.8815	4.0698	NV	
				2,9	0.3691	2.4056	5.7869	4.0698	NV	
				2,10	0.3688	2.0671	4.2727	4.0698	NV	
2019 Dec 17	2458835	R	30	9,10	1.3151	1.2773	1.6315	2.6740	NV	NV
				9,11	0.7377	1.3155	1.7307	2.6740	NV	
				9,12	1.0425	1.0698	1.1445	2.6740	NV	

NOTE—S1 and S2 are the comparison and control star numbers respectively used for the IDV tests. Star numbers follow the star maps shown in Table 5.

Table 7. Result of power enhanced F-test and nested ANOVA test for IDV on AO 0235+164 differential lightcurves from CASLEO and CAHA

Obs. date	Band	No. of Obs.	Power enhanced F-test				Nested ANOVA test			Status	Variability amplitude(%)	doubling timescale (days)
			Comp. star	DOF(ν_1,ν_2)	F_{enh}	$F_c^{0.005}$	DOF(ν_1,ν_2)	F	$F_c^{0.005}$			
1999 Nov 2	V	23	2	(22, 87)	116.132	2.209	(5, 17)	58.924	5.075	V	43.99	0.103
1999 Nov 3	V	22	2	(21, 42)	34.529	2.540	(5, 16)	10.920	5.212	V	24.47	0.145
1999 Nov 4	V	30	2	(29, 58)	86.046	2.216	(7, 22)	38.922	4.109	V	34.48	0.106
	R	30		(29, 58)	82.016	2.216	(7, 22)	40.356	4.109	V	32.59	0.083
1999 Nov 5	V	22	2	(21, 21)	9.207	3.216	(5, 16)	4.426	5.212	NV	10.94	0.140
	R	23		(22, 44)	2.951	2.487	(5, 17)	9.426	5.075	V	9.03	0.335
1999 Nov 6	V	29	2	(28, 166)	211.363	1.960	(7, 21)	58.114	4.179	V	36.79	0.092
	R	30		(29, 170)	107.913	1.941	(7, 22)	74.686	4.109	V	37.90	0.085
1999 Nov 7	V	12	2	(11, 55)	6.392	2.854	–	–	–	PV	9.13	0.170
	R	11		(10, 50)	6.413	2.988	–	–	–	PV	5.36	0.244
2000 Dec 21	V	10	2	(9, 54)	4.813	3.055	–	–	–	PV	6.95	0.275
	R	10		(9, 54)	6.73	3.055	–	–	–	PV	7.67	0.428
2000 Dec 23	V	11	2	(10, 70)	10.314	2.846	–	–	–	PV	20.58	0.200
	R	10		(9, 63)	14.542	2.989	–	–	–	PV	14.18	0.180
2001 Nov 9	V	12	2	(11, 54)	2.345	2.863	–	–	–	NV	12.13	0.372
	R	12		(11, 22)	5.91	3.612	–	–	–	PV	12.73	0.441
2001 Nov 10	V	10	2	(9, 27)	1.152	3.557	–	–	–	NV	8.49	0.227
	R	10		(9, 27)	1.054	3.557	–	–	–	NV	5.64	0.660
2001 Nov 11	V	14	2	(13, 38)	2.02	2.923	–	–	–	NV	9.63	0.364
	R	14		(13, 38)	2.02	2.923	–	–	–	NV	9.63	0.364
2001 Nov 12	V	12	2	(11, 44)	2.212	2.969	–	–	–	NV	12.06	0.539
	R	12	2	(11, 22)	3.928	3.612	–	–	–	PV	11.74	0.856
2001 Nov 13	V	11	3	(10, 10)	0.470	5.847	–	–	–	NV	10.81	0.160
	R	11	3	(10, 10)	1.307	5.847	–	–	–	NV	10.19	0.178
2005 Jan 16	R	11	2	(10, 40)	9.842	3.117	–	–	–	PV	32.92	0.095
2005 Nov 2	R	32	2	(31, 247)	27.709	1.868	(7, 24)	37.156	3.991	V	8.98	0.189
2005 Nov 4	R	12	2	(11, 88)	31.995	2.689	–	–	–	V	6.59	0.166
2005 Nov 5	R	44	2	(43, 343)	124.459	1.713	(10, 33)	16.301	3.26	V	13.60	0.146
2005 Nov 6	R	40	2	(39, 273)	57.755	1.767	(9, 30)	87.95	3.45	V	9.79	0.227
2005 Nov 8	R	28	2	(27, 182)	4.371	1.965	(6, 21)	0.449	4.393	PV	3.18	0.365
2005 Dec 5	R	20	2	(19, 133)	1.067	2.200	(4, 15)	14.394	5.803	PV	2.61	0.391
2005 Dec 6	R	16	2	(15, 120)	4.863	2.373	–	–	–	PV	3.53	0.746
2019 Dec 17	R	30	9	(29, 87)	1.453	2.075	(7, 22)	2.341	4.109	NV	7.74	0.038

NOTE—Comparison star numbers follow the star maps shown in Table 5.

to be affected only by instrumental fluctuations as any known or suspected variable star can be discarded.

Jang & Miller (1997) and Romero et al. (1999) introduced a parameter C defined as $C = \sigma_{\mathrm{B-S1}}/\sigma_{\mathrm{S2-S1}}$, where $\sigma_{\mathrm{B-S1}}$ and $\sigma_{\mathrm{S2-S1}}$ are the standard deviations in blazar DLC and control star DLC, respectively. The blazar is considered to be variable with 99.5 per cent

confidence level if C is greater than a critical value of 2.576.

Howell et al. (1988) pointed out that it is important to select non-variable stars with magnitudes close to the blazar magnitude as comparison and control stars. Otherwise, even if the blazar is non-variable, there will be difference between $\sigma_{\mathrm{B-S1}}$ and $\sigma_{\mathrm{S2-S1}}$ due to dif-
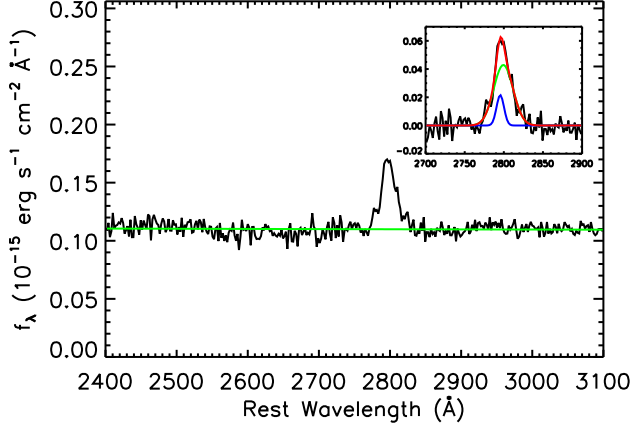
Figure 9. Spectral fitting of AO 0235+164, where the black line is the original spectrum while the green line is the single power law for the fitted continuum. The inset shows Mg II line fitting where the blue, green, and red lines are the narrow, broad, and total components, respectively.

ferences in photon statistics and other random-noise terms (sky, read-out noise). To use field stars with different magnitude levels, Howell et al. (1988) suggests calculating a correction factor Γ to scale σ_{S2-S1} to the instrumental level of σ_{B-S1} for proper comparison. Γ can be estimated using the following formula:

$$\Gamma^2 = \left(\frac{N_{S2}}{N_B}\right)^2 \left[\frac{N_{S1}^2(N_B + P) + N_B^2(N_{S1} + P)}{N_{S2}^2(N_{S1} + P) + N_{S1}^2(N_{S2} + P)}\right] \quad (7)$$

where N is the total (sky-subtracted) counts within the aperture, while the sub-indices B, S1 and S2 correspond to N of the blazar, comparison star and control star, respectively. The factor P contains the common noise-terms, as $P = n_{pix}(N_{sky} + N_{RON}^2)$, where n_{pix} is the number of pixels within the aperture, N_{sky} is the sky level and N_{RON} is the read-out noise. We used the median values of N of the objects and sky for calculating Γ. Thus, the scaled C parameter (C_Γ) is defined as

$$C_\Gamma = \frac{C}{\Gamma} = \frac{1}{\Gamma}\left(\frac{\sigma_{B-S1}}{\sigma_{S2-S1}}\right). \quad (8)$$

The source is considered variable if $C_\Gamma \geq 2.576$. Even though the C parameter is not a proper statistic, it remains a useful indicator of stability (de Diego 2014; de Diego et al. 2015; Zibecchi et al. 2017, 2020).

3.2.2. Scaled F-test

The standard F-statistics parameter is $F = \sigma_{B-S1}^2/\sigma_{S2-S1}^2$, where σ_{B-S1}^2 and σ_{S2-S1}^2 are the variances in blazar DLC and a control star DLC respectively. The scaled F-statistics F_Γ is given as

$$F_\Gamma = \frac{F}{\Gamma^2} = \frac{1}{\Gamma^2}\left(\frac{\sigma_{B-S1}^2}{\sigma_{S2-S1}^2}\right).$$

The F-statistic assumes that the uncertainties in the observations are normally distributed. If $n_{(B-S1)}$ and $n_{(S2-S1)}$ are the sizes of the blazar and control star DLC respectively, the number of degrees of freedom in the numerator and denominator of the F-statistic are $\nu_1 = n_{(B-S1)} - 1$ and $\nu_2 = n_{(S2-S1)} - 1$, respectively. We calculated F_Γ and considered the blazar to be variable with 99.5 per cent confidence if F_Γ was greater than the critical value $F_c^\alpha(\nu_1, \nu_2)$ at $\alpha = 0.005$ (Zibecchi et al. 2017, 2020).

3.2.3. Power-enhanced F-test

The power-enhanced F -test (PEF) has been used in various recent blazar IDV studies (Pandey et al. 2019; Pandey et al. 2020, and references therein). The power-enhanced F-statistic has the advantage of comparing the blazar variance to the combined variance of multiple field stars and is given as (de Diego 2014)

$$F_{enh} = \frac{s_{blz}^2}{s_c^2}, \quad (9)$$

where s_{blz}^2 is the variance of the DLC of the blazar with respect to a reference star, and s_c^2 is the combined variance of the comparison stars' DLCs with respect to the reference star. Thus, s_c^2 is given as

$$s_c^2 = \frac{1}{\left(\sum_{j=1}^k n_j\right) - k} \sum_{j=1}^k \sum_{i=1}^{n_j} s_{j,i}^2. \quad (10)$$

Here, k is the total number of available comparison stars in the DLC, n_j is the number of observations of the jth comparison star, and $s_{j,i}^2$ is the scaled square deviation of the ith observation of the jth comparison star given as

$$s_{j,i}^2 = \Gamma_j(m_{j,i} - \bar{m}_j)^2. \quad (11)$$

Here Γ_j is the scale factor of the jth comparison star DLC computed following Equation 7.

Using the data of the field stars, we first checked the star–star DLCs to identify any spikes due to instrumental errors or improper removal of cosmic rays, and removed them iteratively if they were more than 3 standard deviations from the mean magnitude. We considered a "well-behaved" star with low fluctuations and an average magnitude close to the blazar as the reference star. The number of degrees of freedom in the numerator and denominator of the F-statistics are

$\nu_1 = n_{\text{blz}} - 1$ and $\nu_2 = \left(\sum_{j=1}^{k} n_j\right) - k$, respectively. We calculated F_{enh}, and considered the blazar to be variable (V) with 99.5 percent confidence if F_{enh} was greater than the critical value $F_c(\nu_1, \nu_2)$ at $\alpha = 0.005$.

3.2.4. *Nested ANOVA test*

In the nested analysis of variance (ANOVA) test, DLCs of the blazar are generated with respect to all the comparison stars used as reference stars. The details of this method are given in de Diego et al. (2015). The nested ANOVA test needs a large number of points in the light curves, strongly limiting its application to densely populated DLCs. We divided the DLCs with at least 20 observations into groups such that each group contains 4 observations. Equation (4) of de Diego et al. (2015) considers an ideal set of lightcurves where the total number of observations are divisible by the group size. In most of the DLCs in this work, the total number of observations was not an integral multiple of the group size of 4. So, in those cases, the last group contained less than 4 observations, and we calculated the degrees of freedom accordingly to compute the mean square due to groups (MS_G) and mean square due to the nested observations in groups ($\text{MS}_{O(G)}$). The ANOVA F-statistic is given as, $F = \text{MS}_G/\text{MS}_{O(G)}$. For a significance level of $\alpha = 0.005$, if the F-statistic is greater than the critical value (F_c), the blazar is taken as variable (V), otherwise as non-variable (NV) with 99.5 per cent confidence.

We have listed the results of the scaled C-criterion and scaled F-test in Table 6 and those of power enhanced F-test and the nested ANOVA test in Table 7. In the case of scaled C-criterion and F-test, we fixed one particular star as the comparison star for each dataset. The source is declared variable with respect to one comparison-control star pair if both scaled C-statistics and F-statistics cross their respective critical values. We declare the final variability status of the blazar as variable/non-variable (V/NV) if it is variable/non-variable against all control stars. If the blazar is variable against some of the control stars, we call it probably variable (PV). We did not carry out the nested ANOVA test in a few datasets containing less than 20 observations. In the case of the power-enhanced F-test in absence of the corresponding nested ANOVA test, we call the blazar probably variable (PV) even if the F-statistic crosses the critical value, as the F-test is more prone to give a false positive result (Zibecchi et al. 2017, 2020). If nested ANOVA is present and both the tests cross the critical values, we call the blazar variable (V). Otherwise, we declare the source non-variable (NV). We list the summary of the IDV tests in Table 8. We give

a final verdict on the variability status of the source after comparing the results of the combination of the C-test and F-test (C&F) from Table 6 and results of the combination of the power-enhance F-test and nested ANOVA test (P&N) from Table 7. If the results from both combinations were the same, we kept that result. If C&F declared "V" and P&N declared "PV" due to the absence of nested ANOVA, we finally consider the source variable (V). We considered variability on 2005 November 8 as "NV" because both C-test and nested ANOVA resulted in non-variability. Despite being variable in nested ANOVA, we consider the 2005 December 5 lightcurve "NV" as the F-test and PEF-test detected no variability. A few examples of DLCs of AO 0235+164 having different variability characteristics (V/PV/NV) are shown in Figure 8.

3.2.5. *Doubling timescale*

A flux doubling/halving timescale gives an estimate of the variability timescale (τ_{var}) of a source. We calculate the flux doubling/halving timescale (τ_d) between two consecutive observations and its corresponding significance (σ) as

$$\begin{aligned} \mathcal{F}(t_{i+1}) &= \mathcal{F}(t_i) * 2^{(t_{i+1} - t_i)/\tau_d} \\ \sigma &= |\mathcal{F}(t_{i+1}) - \mathcal{F}(t_i)|/\varepsilon_i, \end{aligned} \tag{12}$$

where $\mathcal{F}(t_i)$ and ε_i are the flux observed at time t_i and the corresponding measurement uncertainty, respectively. We consider the fastest doubling timescale (τ_d^{min}) with a higher significance than 3σ as an estimate for τ_{var}. We obtained $\tau_d^{\text{min}} < 1$ day for all the nights when the source showed significant IDV both in scaled F-test and nested ANOVA test. This further strengthens our claims for the frequent presence of IDV. Following Equation 2 we computed the variability amplitudes on the same nights. All these results are listed in Table 7.

3.2.6. *Duty cycle*

We calculated the duty cycle (DC) of AO 0235+164 using the definition of Romero et al. (1999), that was used later by multiple authors (e.g., Stalin et al. 2009; Agarwal et al. 2016). The formula for DC for a particular waveband is given as,

$$\text{DC} = 100 \frac{\sum_{i=1}^{n} N_i (1/\Delta t_i)}{\sum_{i=1}^{n} (1/\Delta t_i)} \% \tag{13}$$

where $\Delta t_i = \Delta t_{i,obs}/(1+z)$ (duration of the monitoring session on i^{th} night is $\Delta t_{i,obs}$). Thus, this formula calculates the duty cycle weighted by the cosmological redshift corrected monitoring duration of each night. We set $N_i = 1, 0.5$, and 0 for the nights with variability

Table 8. Summary of statistical tests for IDV on AO 0235+164 differential lightcurves from CASLEO and CAHA

Obs. date	Band	Combined variability status		Final status
		$(C$ & F-test$)^a$	(PEF & N-ANOVA$)^b$	
1999 Nov 2	V	V	V	V
1999 Nov 3	V	V	V	V
1999 Nov 4	V	V	V	V
	R	V	V	V
1999 Nov 5	V	V	NV	PV
	R	NV	V	PV
1999 Nov 6	V	V	V	V
	R	V	V	V
1999 Nov 7	V	PV	PV	PV
	R	PV	PV	PV
2000 Dec 21	V	PV	PV	PV
	R	PV	PV	PV
2000 Dec 23	V	PV	PV	PV
	R	V	PV	V
2001 Nov 9	V	NV	NV	NV
	R	V	PV	V
2001 Nov 10	V	NV	NV	NV
	R	NV	NV	NV
2001 Nov 11	V	NV	NV	NV
	R	NV	NV	NV
2001 Nov 12	V	NV	NV	NV
	R	PV	PV	PV
2001 Nov 13	V	NV	NV	NV
	R	NV	NV	NV
2005 Jan 16	R	V	PV	V
2005 Nov 2	R	V	V	V
2005 Nov 4	R	V	V	V
2005 Nov 5	R	V	V	V
2005 Nov 6	R	V	V	V
2005 Nov 8	R	NV	PV	NV
2005 Dec 5	R	NV	PV	NV
2005 Dec 6	R	PV	PV	PV
2019 Dec 17	R	NV	NV	NV

Note—^{a}Table 6, ^{b}Table 7, PEF=power-enhanced F-test.

status "V", "PV", and "NV" respectively. We obtained the duty cycle of AO 0235+164 to be ∼44 percent in V-band, and ∼45 percent in R-band considering the nights where the source was observed for at least 2 hours.

3.3. *The mass of the central black hole*

We estimate the mass of the SMBH in AO 0235+164 by using its spectrum observed using the CCD Imaging/Spectropolarimeter (SPOL) at the Steward Observatory[4] on 2011 January 8 (air mass = 1.12). This spectrum was selected since the blazar was then at its lowest level during the period 2008–2018, and should ensure the best visibility of the emission lines because of the lower continuum contribution from the jet. The observed wavelength range of the spectrum we used is 4000–7550 Å, with a spectral resolution of 4 Å, and it is analyzed by following the procedure given in Liao & Gu (2020). Firstly, it was corrected for Galactic extinction with the reddening map of Schlegel et al. (1998), and then was shifted to the rest-frame wavelength by using the redshift of 0.94.

This spectral coverage meant we could use the Mg II line, which is prominent on the spectrum shown in Figure 9 (focused on the 2400−3100 Å range), to estimate the SMBH mass. We modeled the continuum by applying a single power law ($f_\lambda \propto \lambda^\alpha$) (as Fe II emission is rather weak). A Gaussian profile was then used to fit the Mg II line, centered at the position of 2800 Å, on the continuum-subtracted spectrum. The broad component of Mg II was fitted with a Gaussian with a $1000 \, \mathrm{km \, s^{-1}}$ lower limit, while a Gaussian with upper limit of $1000 \, \mathrm{km \, s^{-1}}$ was applied for the narrow component. In order to estimate the corresponding errors of full width at half maximum (FWHM) and flux, we generated 100 mock spectra by adding random Gaussian noise to the original spectrum using the flux density errors, and then took the standard deviation of measurements from those mock spectra as the uncertainties. Here, the flux density errors were the RMS value of the spectrum calculated over the spectral window of (3000−3100) Å, after subtracting a second-order polynomial function. Figure 9 shows the resulting fit to the spectrum. Our best fitting results indicate that the line width of the broad Mg II component is FWHM = 3151 $\mathrm{km \, s^{-1}}$, with log-scale luminosity in erg s^{-1}, $\log(L_{\mathrm{MgII}})$ = 42.8.

The line width and the Mg II line luminosity we find are consistent with the range of values FWHM=3100–3500 $\mathrm{km \, s^{-1}}$ and $\log(L_{\mathrm{MgII}})$=42.5–42.8, respectively, which were derived by Raiteri et al. (2007) from one VLT and four TNG spectra of AO 0235+164 acquired in 2003–2004. We use the FWHM and luminosity of the broad Mg II line, not the continuum luminosity, as
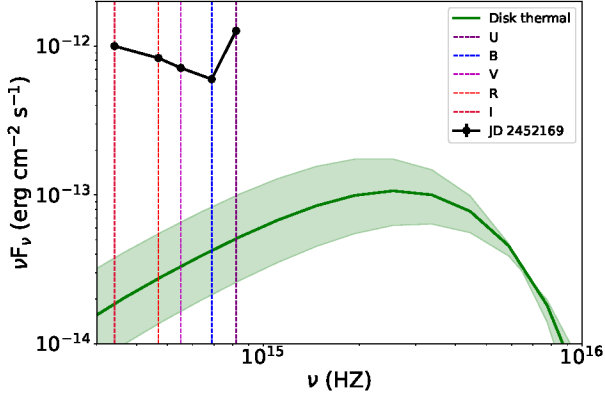
Figure 10. Comparison of the SED of the lowest flux state observed on JD 2452169 and the thermal emission from the accretion disk in the observer's frame. The thermal emission component is calculated using a multi-temperature disk model with the black hole mass $\log(M_{\mathrm{BH}}/M_\odot) = 7.9 \pm 0.25$, and the log-scale disk luminosity in erg s^{-1}, $\log(L_{\mathrm{disk}}) = 45.01 \pm 0.20$. The shaded region indicates the uncertainties in the calculation of the disk thermal component.

we are unable to exclude the jet emission contribution, despite the low state spectrum that we could use for this blazar. The black hole mass is derived from the empirical relation used for Mg II (Kong et al. 2006), which is based on measured broad line region sizes in the reverberation-mapping AGN sample of Peterson et al. (2004), as

$$\frac{M_{\mathrm{BH}}}{M_\odot} = 2.9 \times 10^6 \left(\frac{L_{\mathrm{MgII}}}{10^{42} \text{ erg s}^{-1}} \right)^{0.57 \pm 0.12} \left(\frac{\mathrm{FWHM}_{\mathrm{MgII}}}{10^3 \text{ km s}^{-1}} \right)^2 \tag{14}$$

Thus, the SMBH mass is $\log(M_{\mathrm{BH}}/M_\odot) = 7.90 \pm 0.25$, where the uncertainty is estimated from the measurement uncertainties of the FWHM and luminosity of Mg II. Using optical spectroscopy data from the SDSS archive, Paliya et al. (2021) reported a somewhat higher mass, $\log(M_{\mathrm{BH}}/M_\odot) = 8.58 \pm 0.34$, and an accretion disk luminosity (in erg s^{-1}), of $\log(L_{\mathrm{disk}}) = 45.30 \pm 0.22$. Using the method mentioned in Paliya et al. (2021) with $\log(L_{\mathrm{MgII}}) = 42.8$, we obtained a lower disk luminosity (in erg s^{-1}) of $\log(L_{\mathrm{disk}}) = 45.01 \pm 0.20$ from the spectrum observed on 2011 January 8.

4. DISCUSSION

In this work, we have presented a detailed temporal and spectral study of the highly variable emission from the blazar AO 0235+164 observed at multiple optical wavebands (*UBVRI*) from October 1975 to December 2019. The lightcurves have highly uneven data sampling due to gaps in observation seasons and non-uniform observation campaigns. Although *U*-band data are quite

sparsely sampled the *BVRI* observations have denser sampling when the source was highly active. Multiple long-term studies suggested that AO 0235+164 shows ~2-year long flaring episodes with multiple sub-flares after intervals of ~8 years (Raiteri et al. 2006; Fan et al. 2017; Roy et al. 2022). Figure 1 shows a difference of about six magnitudes between the quiescent and outburst states in all optical wavebands, corresponding to an energy flux variation of more than two orders of magnitude (Figure 6). The long-term variability amplitudes at all five wavebands are quite similar (Table 1). Also, we found a strong correlation with zero time-lag between the *UBVI* observations and the *R*-band data (Figure 2 and Figure 3), which implies a common radiative process at a single emission zone is responsible for the bulk of the emission at the optical wavebands.

Sometimes during the quiescent states of powerful blazars, the disk thermal emission component becomes visible as a big blue bump on top of the synchrotron emission component from the jet in the optical-UV wavebands (e.g., Roy et al. 2021). As the disk emission is bluer than the jet synchrotron emission, an increase in the jet activity during low flux states displays a redder-when-brighter trend. The enhanced jet activity is observed when the charged particles inside the jet get accelerated to higher energies, and then radiate faster. Thus, the jet synchrotron component tends to get bluer with the increase in flux. If the jet emission completely outshines the disk emission, we expect to see a bluer-when-brighter trend (e.g., Isler et al. 2017). The flux increment can also be attributed to the increase in the jet Doppler factor (e.g., Papadakis et al. 2007), which blueshifts the spectrum and produces a bluer-when-brighter trend because of the convexity of the spectrum. Such a trend is seen in the $(B-I)$ vs R magnitude diagram (Figure 4b) and indicates the domination of non-thermal jet emission over the thermal emission component of the accretion disk during both flaring and quiescent states. From the convex shapes of the optical *BVR* SEDs during states ranging from quiescent to flaring (see the accompanying SED video and Figure 6), we may infer that the effect of the disk thermal emission is not significant in optical wavebands even during the low flux states.

This can be explained in terms of the nature of disk thermal emission given the disk luminosity and the central black hole mass computed in subsection 3.3. The primary, and most precise, black hole mass estimation methods are based on stellar and gas kinematics and reverberation mapping (e.g. Vestergaard 2004). These

methods need high spatial resolution spectroscopy data from the host galaxy and/or higher ionization emission lines and are not applicable to most BL Lacertae objects (BL Lacs). But in BL Lacs, if the weak emission lines are present, we can use the empirical methods (Kong et al. 2006) for BH mass estimation. The most common methods used for BH mass estimation for BL Lacs are the shortest variability timescales and periods of QPOs (Gupta et al. 2012). Since BL Lacs are highly variable objects, any BH mass estimation may be treated as an upper limit, and there are possibilities of detection of a shorter variability timescale or shorter QPO period. We obtained a log-scale BH mass of 7.90±0.25 in solar mass unit. The Steward observatory spectrum we used in our analysis had a narrower Mg II emission line (FWHM=3151 km s^{-1}) than those of Raiteri et al. (2007) and Paliya et al. (2021), thus resulting in a lower mass estimate. We considered a multi-temperature blackbody type accretion disk model, where the temperature at any portion of the disk is a function of the disk luminosity and the central black hole mass, to compute the thermal emission component. In Figure 10 we plotted the thermal component along with the optical-UV SED during the lowest activity state of AO 0235+164 observed on JD 2452169. It is evident that, as the thermal emission peaks at far UV frequencies ($\sim3.5\times10^{15}$ Hz) in the observer's frame of reference, the jet emission always dominates in $BVRI$ wavebands. We do not see any significant trend in the variation of the $(V - R)$ spectral index (α_{VR}) (Figure 7). The sudden rise of the U-band flux in Figure 10 is an indicator of a probable UV-soft X-ray bump as discussed in Raiteri et al. (2005, 2006). According to these studies, the source of the bump is either an additional synchrotron component coming from a separate emission region in the jet or the emission of a continuous inhomogeneous jet is suppressed in near UV region due to a discontinuity in opacity or misalignment of that particular emission region. Ackermann et al. (2012) mentioned that the whole optical-UV spectrum is produced by a single synchrotron emitting zone as the shape of the bump does not change with luminosity. They attributed the UV spectral hardening to an artifact due to the overestimation of extinction by Junkkarinen et al. (2004).

For the detection of any statistically significant intraday variability in 33 lightcurves of AO 0235+164 observed at CASLEO/CAHA, we employed different statistical tests widely used in AGN variability studies. The reliability of each of these tests has been disputed (e.g. de Diego et al. 2015; Zibecchi et al. 2017), so we here employed a comparative approach that could allow us to circumvent the limitations affecting any individual test. In the first place, we used the scaled C-criterion and the F-test. The first compares the dispersion of the blazar lightcurve to the dispersion of a field star (control star), while the latter does so with the variances. According to Zibecchi et al. (2017) and Zibecchi et al. (2020), the F-test has a tendency to classify noisy nonvariable curves as a variable (i.e., give false positives), while the C-criterion tends to give false negatives. Even though the C-criterion (Romero et al. 1999) cannot be considered as an actual statistical test, it may still be a useful parameter to detect variability with high significance. The F-test, on the other hand, does not always work as expected, because it is particularly sensitive to non-Gaussian errors ("red noise"), which are usually an issue when analyzing blazars DLCs.

We also used the power-enhanced F-test and the nested ANOVA test, which involve multiple field stars. It is expected that the power-enhanced F-test may also suffer from the same drawback of detecting false variability as the (original) F-test. In the nested ANOVA test, in turn, data grouping may lead to false results if data within a time span larger than the (unknown) variability timescale are grouped. Comparing the results of Table 6 and Table 7, while considering the tendencies of giving false results by the respective tests, we can confirm that the source was significantly variable in 4 out of 13 V-band lightcurves, and 9 out of 20 R-band lightcurves. The source seems to be probably variable in 3 V-band and 4 R-band lightcurves, and non-variable in the rest. On 1999 November 5, the combination of C-criterion and F-test indicates non-variability but the combination of power-enhanced F-test and nested ANOVA detects variability in the R-band lightcurve. The results in the V-band lightcurve on that day are exactly the opposite. Similar situations were observed also on 2001 November 9 and 2001 November 12. A visual inspection of the DLCs of these nights reveals that the blazar DLCs were classified as non-variable when either the control star DLC had higher variability (1999 November 5) or the measurement errors of the blazar DLCs were higher due to its low-flux state (2001 November 9 and 12). Higher measurement errors lead to a lower chance of significant variability detection. These strange results may be an example of the drawbacks of the applied methods when trying to recover low-amplitude variations from DLCs affected by non-Gaussian noise (part of the observations on that night were taken at air mass > 2 and under non-photometric conditions). Otherwise, the combined results of different methods seem to more or less agree. Alongside the optical SED patterns, such frequent IDV establishes AO 0235+164 as a low-energy

Table 9. Variation of duty cycle with the duration of observation in R-band.

Observation duration (hours)	No. of nights	Duty cycle (%)
> 1	20	52
> 2	19	45
> 3	17	50
> 4	14	57
> 5	13	64
> 6	8	77

peaked BL Lac (LBL) object. High energy peaked BL Lacs (HBL) show significantly less optical intraday variability than the LBLs (Heidt & Wagner 1998; Romero et al. 1999).

The differences in IDV behavior have been attributed to the strength of magnetic fields present in the jet of HBLs. A higher axial magnetic field (B) than a critical value (B_c) may prevent the generation of any bends and Kelvin-Helmhotz instabilities in the jet-base responsible for creating intraday microvariabilities. This indicates the presence of a weaker magnetic field than B_c in the jet of AO 0235+164. The critical magnetic field (B_c) is given in Romero (1995) as

$$B_c = \sqrt{4\pi n_e m_e c^2 (\Gamma^2 - 1)}/\Gamma, \qquad (15)$$

where n_e is the electron density in the emission region, m_e is the electron rest mass, and here Γ is the bulk Lorentz factor of the jet flow. Considering a typical set of parameters, $n_e = 429$ cm^{-3} and $\Gamma = 20$ (Ackermann et al. 2012), we get $B_c \simeq 0.07$ G.

From Table 7 and Figure 8, we can say that the variability amplitudes were higher in the 1999 season when the source was in a fainter state (higher magnitude) than its brighter state in the 2005 season. Marscher (2013) suggested that enhancement of flux can arise from a more uniform flow of particles inside the jet, which in turn decreases the amplitude of microvariability associated with the turbulence inside the jet. Equation 9 indicates that the probability of detection of significant variability increases with the duration of observation. Similar results for other blazars were found by Gupta & Joshi (2005), Rani et al. (2010), and Agarwal et al. (2016).

From the flux doubling timescales listed in Table 7, we can estimate the upper limit to the size of the emission region (R_{max}) using the light travel-time argument given as

$$R_{\mathrm{max}} = \frac{c\delta t_{\mathrm{var}}}{1+z} \qquad (16)$$

where z is the cosmological redshift of 0.94, t_{var} is the variability timescale, and δ is the Doppler boost of the jet. Considering $\delta = 24$ (Hovatta et al. 2009) and t_{var} to be the shortest flux doubling timescale of 0.083 days (when the source was significantly variable), we obtain an emission region size upper limit of $\sim 2.6 \times 10^{15}$ cm. Assuming a conical jet model where the emission region fills up the entire jet cross-section, we can estimate the probable maximum distance (d_{max}) of the emission region from the central black hole as, $d_{\mathrm{max}} = \Gamma R_{\mathrm{max}} = 5.2 \times 10^{16}$ cm. To explain the observed strong variability, Marchesini et al. (2016) attempted to apply a swinging jet model that attributes the observed variability to a change in the viewing angle of the emission region with time (i.e. variation in the associated bulk Doppler factor). They reported a high rate of change in viewing angle of about $7-10$ arcmin per day, considering a mean viewing angle of $2.3°$, would be necessary. However, they found that this geometric wiggling-jet scenario was disfavored when considering the observed variation in color index with time. Several earlier studies on AO 0235+164 associated the observed fast optical variability with gravitational microlensing by the foreground absorber at $z = 0.524$. Webb et al. (2000) proposed that the 1997 flare resulted due to microlensing because of an observed correlation with zero lag between radio and optical lightcurves following Stickel et al. (1988), but the absence of any correlated flare in the X-ray lightcurve makes this explanation less likely. Abraham et al. (1993) and Raiteri et al. (2007) explained that such microlensing events can produce small amounts of fast flux amplification but are unlikely to dominate the high variability observed in AO 0235+164.

5. CONCLUSIONS

In this work, we conducted a study of long-term and short-term (intraday) variability in the optical multiwaveband observations of the blazar AO 0235+164. Here we summarize our results and the probable physical scenarios.

1. We observed a variation of about six magnitudes between the quiescent and flaring episodes, or over two orders of magnitude variation in the SEDs.

2. *UBVI* lightcurves are highly correlated with the R-band lightcurve with zero time lag.

3. A significant bluer-when-brighter trend is observed in the $(B - I)$ color variation with R-magnitude.

4. All the optical BVR-band SEDs show convexity. These observations indicate that the optical emission is dominated by jet radiation.

5. AO 0235+164 frequently shows statistically significant intraday variability in optical wavebands. This implies that AO 0235+164 is an LBL and probably has a weak magnetic field in the jet environment.

6. From the analysis of a broad Mg II emission line in a spectrum of AO 0235+164 taken at a low state, we estimate a central black-hole mass of $\sim 7.9 \times 10^7 M_\odot$.

Software: Astropy (Astropy Collaboration et al. 2013), DAOPHOT (Stetson 1987), IRAF (Tody 1986)

REFERENCES

Abraham, R. G., Crawford, C. S., Merrifield, M. R., Hutchings, J. B., & McHardy, I. M. 1993, ApJ, 415, 101, doi: 10.1086/173147

Ackermann, M., Ajello, M., Ballet, J., et al. 2012, ApJ, 751, 159, doi: 10.1088/0004-637X/751/2/159

Ackermann, M., Ajello, M., Ballet, J., et al. 2012, ApJ, 751, doi: 10.1088/0004-637X/751/2/159

Agarwal, A., Gupta, A. C., Bachev, R., et al. 2016, MNRAS, 455, 680, doi: 10.1093/mnras/stv2345

Agudo, I., Marscher, A. P., Jorstad, S. G., et al. 2011, ApJL, 735, L10, doi: 10.1088/2041-8205/735/1/L10

Astropy Collaboration, Robitaille, T. P., Tollerud, E. J., et al. 2013, A&A, 558, A33, doi: 10.1051/0004-6361/201322068

Bessell, M. S. 2005, ARA&A, 43, 293, doi: 10.1146/annurev.astro.41.082801.100251

Bonning, E., Urry, C. M., Bailyn, C., et al. 2012, The Astrophysical Journal, 756, 13, doi: 10.1088/0004-637X/756/1/13

Cellone, S. A., Romero, G. E., Combi, J. A., & Martí, J. 2007, MNRAS, 381, L60, doi: 10.1111/j.1745-3933.2007.00366.x

Cohen, R. D., Smith, H. E., Junkkarinen, V. T., & Burbidge, E. M. 1987, ApJ, 318, 577, doi: 10.1086/165393

de Diego, J. A. 2014, AJ, 148, 93, doi: 10.1088/0004-6256/148/5/93

de Diego, J. A., Polednikova, J., Bongiovanni, A., et al. 2015, AJ, 150, 44, doi: 10.1088/0004-6256/150/2/44

Edelson, R. A., & Krolik, J. H. 1988, ApJ, 333, 646, doi: 10.1086/166773

Fan, J. H., & Lin, R. G. 1999, ApJS, 121, 131, doi: 10.1086/313191

Fan, J. H., Tao, J., Qian, B. C., et al. 2006, Publications of the Astronomical Society of Japan, 58, 797, doi: 10.1093/pasj/58.5.797

Fan, J. H., Kurtanidze, O., Liu, Y., et al. 2017, ApJ, 837, 45, doi: 10.3847/1538-4357/aa5def

Fossati, G., Maraschi, L., Celotti, A., Comastri, A., & Ghisellini, G. 1998, MNRAS, 299, 433, doi: 10.1046/j.1365-8711.1998.01828.x

González-Pérez, J. N., Kidger, M. R., & Martín-Luis, F. 2001, AJ, 122, 2055, doi: 10.1086/322129

Guo, Y. C., Hu, S. M., Xu, C., et al. 2015, NewA, 36, 9, doi: 10.1016/j.newast.2014.09.011

Gupta, A. C., Banerjee, D. P. K., Ashok, N. M., & Joshi, U. C. 2004, A&A, 422, 505, doi: 10.1051/0004-6361:20040306

Gupta, A. C., Fan, J. H., Bai, J. M., & Wagner, S. J. 2008, AJ, 135, 1384, doi: 10.1088/0004-6256/135/4/1384

Gupta, A. C., & Joshi, U. C. 2005, A&A, 440, 855, doi: 10.1051/0004-6361:20042370

Gupta, S. P., Pandey, U. S., Singh, K., et al. 2012, NewA, 17, 8, doi: 10.1016/j.newast.2011.05.005

Hagen-Thorn, V. A., Larionov, V. M., Jorstad, S. G., et al. 2008, ApJ, 672, 40, doi: 10.1086/523841

Heidt, J., & Wagner, S. J. 1996, A&A, 305, 42. https://arxiv.org/abs/astro-ph/9506032

—. 1998, A&A, 329, 853. https://arxiv.org/abs/astro-ph/9709116

Hovatta, T., Valtaoja, E., Tornikoski, M., & Lähteenmäki, A. 2009, A&A, 494, 527, doi: 10.1051/0004-6361:200811150

Howell, S. B., Mitchell, K. J., & Warnock, A. I. 1988, AJ, 95, 247

Ikejiri, Y., Uemura, M., Sasada, M., et al. 2011, PASJ, 63, 639, doi: 10.1093/pasj/63.3.327

Impey, C. D., Brand, P. W. J. L., & Tapia, S. 1982, MNRAS, 198, 1, doi: 10.1093/mnras/198.1.1

Isler, J. C., Urry, C. M., Coppi, P., et al. 2017, The Astrophysical Journal, 844, 107, doi: 10.3847/1538-4357/aa79fc

Itoh, R., Nalewajko, K., Fukazawa, Y., et al. 2016, ApJ, 833, 77, doi: 10.3847/1538-4357/833/1/77

Jang, M., & Miller, H. R. 1997, AJ, 114, 565, doi: 10.1086/118493

Junkkarinen, V. T., Cohen, R. D., Beaver, E. A., et al. 2004, ApJ, 614, 658, doi: 10.1086/423777

Kong, M.-Z., Wu, X.-B., Wang, R., & Han, J.-L. 2006, ChJA&A, 6, 396, doi: 10.1088/1009-9271/6/4/02

Kutkin, A. M., Pashchenko, I. N., Lisakov, M. M., et al. 2018, MNRAS, 475, 4994, doi: 10.1093/mnras/sty144

Landolt, A. U. 2009, AJ, 137, 4186, doi: 10.1088/0004-6256/137/5/4186

Liao, M., & Gu, M. 2020, MNRAS, 491, 92, doi: 10.1093/mnras/stz2981

Madejski, G., Takahashi, T., Tashiro, M., et al. 1996, ApJ, 459, 156, doi: 10.1086/176877

Marchesini, E. J., Andruchow, I., Cellone, S. A., et al. 2016, A&A, 591, A21, doi: 10.1051/0004-6361/201527632

Marscher, A. P. 1983, ApJ, 264, 296, doi: 10.1086/160597

Marscher, A. P. 2013, The Astrophysical Journal, 780, 87, doi: 10.1088/0004-637x/780/1/87

Miller, H. R., Carini, M. T., & Goodrich, B. D. 1989, Nature, 337, 627, doi: 10.1038/337627a0

Mücke, A., Protheroe, R. J., Engel, R., Rachen, J. P., & Stanev, T. 2003, Astroparticle Physics, 18, 593, doi: 10.1016/S0927-6505(02)00185-8

Nilsson, K., Charles, P. A., Pursimo, T., et al. 1996, A&A, 314, 754

Paliya, V. S., Domínguez, A., Ajello, M., Olmo-García, A., & Hartmann, D. 2021, ApJS, 253, 46, doi: 10.3847/1538-4365/abe135

Pandey, A., Gupta, A. C., Wiita, P. J., & Tiwari, S. N. 2019, ApJ, 871, 192, doi: 10.3847/1538-4357/aaf974

Pandey, A., Gupta, A. C., Kurtanidze, S. O., et al. 2020, The Astrophysical Journal, 890, 72, doi: 10.3847/1538-4357/ab698e

Papadakis, I. E., Villata, M., & Raiteri, C. M. 2007, A&A, 470, 857, doi: 10.1051/0004-6361:20077516

Peterson, B. M., Ferrarese, L., Gilbert, K. M., et al. 2004, ApJ, 613, 682, doi: 10.1086/423269

Qian, S. J., Kraus, A., Witzel, A., Krichbaum, T. P., & Zensus, J. A. 2000, A&A, 357, 84

Rabbette, M., McBreen, S., Steel, B., & Smith, N. 1996, A&A, 310, 1

Raiteri, C. M., Villata, M., Capetti, A., et al. 2007, A&A, 464, 871, doi: 10.1051/0004-6361:20066599

Raiteri, C. M., Villata, M., Aller, H. D., et al. 2001, A&A, 377, 396, doi: 10.1051/0004-6361:20011112

Raiteri, C. M., Villata, M., Ibrahimov, M. A., et al. 2005, A&A, 438, 39, doi: 10.1051/0004-6361:20042567

Raiteri, C. M., Villata, M., Kadler, M., et al. 2006, A&A, 459, 731, doi: 10.1051/0004-6361:20065744

Raiteri, C. M., Villata, M., Larionov, V. M., et al. 2008, A&A, 480, 339, doi: 10.1051/0004-6361:20079044

Raiteri, C. M., Villata, M., Acosta-Pulido, J. A., et al. 2017, Nature, 552, 374, doi: 10.1038/nature24623

Rani, B., Gupta, A. C., Strigachev, A., et al. 2010, Monthly Notices of the Royal Astronomical Society, 404, 1992, doi: 10.1111/j.1365-2966.2010.16419.x

Romero, G. E. 1995, Ap&SS, 234, 49, doi: 10.1007/BF00627281

Romero, G. E., Boettcher, M., Markoff, S., & Tavecchio, F. 2017, SSRv, 207, 5, doi: 10.1007/s11214-016-0328-2

Romero, G. E., Cellone, S. A., & Combi, J. A. 1999, A&AS, 135, 477, doi: 10.1051/aas:1999184

—. 2000, A&A, 360, L47. https://arxiv.org/abs/astro-ph/0007407

Romero, G. E., Cellone, S. A., Combi, J. A., & Andruchow, I. 2002, A&A, 390, 431, doi: 10.1051/0004-6361:20020743

Roy, A., Patel, S. R., Sarkar, A., Chatterjee, A., & Chitnis, V. R. 2021, MNRAS, 504, 1103, doi: 10.1093/mnras/stab975

Roy, A., Chitnis, V. R., Gupta, A. C., et al. 2022, MNRAS, 513, 5238, doi: 10.1093/mnras/stac1287

Sagar, R., Stalin, C. S., Gopal-Krishna, & Wiita, P. J. 2004, MNRAS, 348, 176, doi: 10.1111/j.1365-2966.2004.07339.x

Schlegel, D. J., Finkbeiner, D. P., & Davis, M. 1998, ApJ, 500, 525, doi: 10.1086/305772

Schramm, K. J., Borgeest, U., Kuehl, D., et al. 1994, A&AS, 106, 349

Smith, P. S., Balonek, T. J., Heckert, P. A., Elston, R., & Schmidt, G. D. 1985, AJ, 90, 1184, doi: 10.1086/113824

Smith, P. S., Montiel, E., Rightley, S., et al. 2009, arXiv e-prints, arXiv:0912.3621. https://arxiv.org/abs/0912.3621

Stalin, C. S., Kawabata, K. S., Uemura, M., et al. 2009, Monthly Notices of the Royal Astronomical Society, 399, 1357, doi: 10.1111/j.1365-2966.2009.15354.x

Stetson, P. B. 1987, Publications of the Astronomical Society of the Pacific, 99, 191, doi: 10.1086/131977

Stickel, M., Fried, J. W., & Kuehr, H. 1988, A&A, 198, L13

—. 1993, A&AS, 98, 393

Takalo, L. O., Sillanpaeae, A., Valtaoja, E., et al. 1998, A&AS, 129, 577, doi: 10.1051/aas:1998205

Tody, D. 1986, in Society of Photo-Optical Instrumentation Engineers (SPIE) Conference Series, Vol. 627, Instrumentation in astronomy VI, ed. D. L. Crawford, 733, doi: 10.1117/12.968154

Urry, C. M., & Padovani, P. 1995, PASP, 107, 803, doi: 10.1086/133630

Vestergaard, M. 2004, in Astronomical Society of the Pacific Conference Series, Vol. 311, AGN Physics with the Sloan Digital Sky Survey, ed. G. T. Richards & P. B. Hall, 69. https://arxiv.org/abs/astro-ph/0401436

Villata, M., Raiteri, C. M., Kurtanidze, O. M., et al. 2002, A&A, 390, 407, doi: 10.1051/0004-6361:20020662

Villata, M., Raiteri, C. M., Larionov, V. M., et al. 2008, A&A, 481, L79, doi: 10.1051/0004-6361:200809552

Villata, M., Raiteri, C. M., Gurwell, M. A., et al. 2009, A&A, 504, L9, doi: 10.1051/0004-6361/200912732

Wagner, S. J., & Witzel, A. 1995, ARA&A, 33, 163, doi: 10.1146/annurev.aa.33.090195.001115

Wang, Y.-F., & Jiang, Y.-G. 2020, ApJ, 902, 41, doi: 10.3847/1538-4357/abb36c

Webb, J. R., Howard, E., Benítez, E., et al. 2000, AJ, 120, 41, doi: 10.1086/301432

White, R. J., & Peterson, B. M. 1994, PASP, 106, 879,
doi: 10.1086/133456

Wierzcholska, A., Ostrowski, M., Stawarz, Ł., Wagner, S.,
& Hauser, M. 2015, A&A, 573, A69,
doi: 10.1051/0004-6361/201423967

Woo, J.-H., & Urry, C. M. 2002, ApJ, 579, 530,
doi: 10.1086/342878

Zhang, B.-K., Jin, M., Zhao, X.-Y., Zhang, L., & Dai, B.-Z.
2021, Research in Astronomy and Astrophysics, 21, 186,
doi: 10.1088/1674-4527/21/8/186

Zibecchi, L., Andruchow, I., Cellone, S. A., & Carpintero,
D. D. 2020, MNRAS, 498, 3013,
doi: 10.1093/mnras/staa2544

Zibecchi, L., Andruchow, I., Cellone, S. A., et al. 2017,
MNRAS, 467, 340, doi: 10.1093/mnras/stx054